nature portfolio
https://doi.org/10.1038/s41586-026-10999-2

Supplementary information

Gravitational torque drives multidecadal variations in length of day

In the format provided by the authors and unedited

Supplementary Information for: Gravitational torque drives multidecadal variations in length of day

Huifeng Zhang, Mathieu Dumberry

1 Length-of-day variations

Extended Data Fig. 7 shows the observed length-of-day (LOD) changes retrieved from the International Earth Rotation Service (IERS): the 100-day interval C02 series in the time range 1949–1961 is shown by the grey dashed line, and the 1-day interval C04 series in the time range 1962–2022 is shown by the solid line. We remove the contribution to LOD changes caused by changes in Atmospheric Angular Momentum (AAM, blue line) and changes in Oceanic Angular Momentum (OAM, green line). The AAM reconstruction is based on the NCEP (1962–1975) and ECMWF (1976–2022) models and the OAM reconstruction is based on the ECCO (1962–1975) and MPIOM (1976–2022) models, all at 1-day interval. The cleaned LOD signal, after removing the AAM and OAM contributions, is shown by the red line. To remove all remaining sub-annual signals, we build a smooth LOD curve by applying a one-year running average to the pre-1962 raw LOD data and a least-squares spline with one-year knot spacing to the post-1962 cleaned LOD data. Finally, we remove from this smooth LOD signal a linear trend of 1.7 milliseconds per century (ms/cy)[1] caused by the combined effects of lunar tidal friction[2] and glacial isostatic adjustment (GIA)[3], and we also remove the LOD contributions from additional surface barystatic processes[3]. The corrected LOD signal (black line in Extended Data Fig. 7) represents the decadal LOD changes attributable to an exchange of angular momentum between the mantle and core.

To extract the multidecadal LOD changes, we apply a 3rd-order low-pass Butterworth filter with a cutoff period of 30 years to the corrected LOD signal (Extended Data Fig. 8). The time period that is the focus of our study is between 1964–2019. This is the reason why we extended the corrected LOD to 1949 (with the C02 series), to limit the edge-effect in 1964 associated with the low-pass filtering. To limit the edge-effect in 2019, we extended the corrected LOD signal by mirror padding until 2030 (see Extended Data Fig. 8). The filtered LOD series between 1964–2019 (red line in Extended Data Fig. 8) is the multidecadal LOD changes that are the target of our study. The residual signal (blue line) captures the higher frequency decadal LOD variations (periods < 30 yr). Because the temporal resolution of core-mantle torques is limited by both the core surface flow models and seismic observations of inner core rotation, these higher frequency LOD changes likely reflect unresolved, shorter-period torque contributions.

2 Individual realizations of the electromagnetic and topographic torques

Our forward model predictions of the electromagnetic (EM) and topographic torques are built from the probabilistic flow model at the CMB from ref.[4]. We use 400 different realizations of this model and associated realizations of the magnetic field model COVOBS.x2[5]; these are available from the Pygeodyn webpage at https://geodyn.univ-grenoble-alpes.fr/[6]. Each realization is an equally probable time-history of the core flow consistent with the observed geomagnetic secular variation. For each realization, we compute the EM and topographic torques as described in Methods. Each torque realization is then multiplied by its respective scaling parameter (K_{em} for the EM torque, K_{top} for the topographic torque). Extended Data Fig. 2 shows the 400 forward models of these torque predictions for $K_{\rm em} = 3$ and $K_{\rm top} = 1$, as well as the predictions from the ensemble flow model. For each realization, we have removed the mean torque over the time period 1964–2019.

3 Inner core rotation model

We use the time-history model of the axial rotation angle $\varphi(t)$ of the inner core between 1964–2021 from ref.[7] (Extended Data Fig. 1a). The latter is reconstructed from the travel time differences of seismic waves passing through the inner core between earthquake doublets events. Our time-history model is specified by seven points from the model of ref.[7] that act as anchor points for a cubic spline fit. Specifically, we use their model based on the SSI-COL path for knots placed at 1964, 1972 and 1984, and their better resolved model based on 6 global paths for knots placed at 2000, 2010, 2015 and 2019. To take into account the uncertainty in $\varphi(t)$ in our Bayesian inversion, we further specify an upper and lower Gaussian error at each point, capturing the asymmetric errors about the mean of the model from ref.[7]. Although the model based on 6 global paths has smaller errors, we take a conservative approach and use the errors associated with the SSI-COL path model. The times, mean values and Gaussian errors of each anchor points are given in Supplementary Table 1.

Supplementary Table 1: Anchor points $\phi_{\rm i}$ and upper and lower error bounds of the inner core rotation model.

time	1964	1972	1984	2000	2010	2015	2019
$\boldsymbol{\phi_{\rm i}}$	-3.268	-3.708	-2.718	0.007	0.961	0.786	0.678
σ_ϕ **(upper)**	0.42	0.57	0.16	0.38	0.34	0.41	0.43
σ_ϕ **(lower)**	1.22	0.84	0.16	0.26	0.24	0.12	0.10

For each sample of torque parameters, we pick randomly a set of errors at each anchor point. The value $\varphi(t_i)$ at each point t_i is computed as $\varphi(t_i) = \phi_{\rm i} + \mathcal{N}(0,1)\sigma_\phi$, where we take the upper error σ_ϕ if $\mathcal{N}(0,1) > 0$, and the lower error if $\mathcal{N}(0,1) < 0$. We then compute a cubic spline representation of $\varphi(t)$ based on these $\varphi(t_i)$ values. The 95% confidence interval (CI) computed from 10^4 time-histories of $\varphi(t)$ are shown in Extended Data Fig. 1b, which provide a good match to the time-history and associated error of the model of ref.[7].

For each sample of $\varphi(t)$, we compute the misalignment angle $\alpha(t)$ of the degree 2 order 2 topography of the ICB by numerically integrating

$$\frac{d\alpha}{dt} = \frac{d\varphi}{dt} - \frac{\alpha}{\tau}\,, \tag{S1}$$

where τ is the viscous relaxation time of the inner core. Extended Data Fig. 1c shows the time-histories of $\alpha(t)$ computed from the samples of $\varphi(t)$ of Extended Data Fig. 1b and for an assumed $\tau = 6.0\,$yr.

The time integration of $\alpha(t)$ requires an initial condition at $t_{\rm o} = 1964$. We build this condition by assuming that $\varphi(t)$ prior to $t_{\rm o}$ is a simple periodic sine function of the form

$$\hat{\varphi}(t) = C\sin(\omega(t - t_{\rm o}) + \gamma)\,, \tag{S2}$$

where the amplitude C, frequency ω and phase γ are found by matching φ, $\mathrm{d}\varphi/\mathrm{d}t$ and $\mathrm{d}^2\varphi/\mathrm{d}t^2$ at $t_{\rm o}$. Note that it is only possible to match our sine function when φ and $\mathrm{d}^2\varphi/\mathrm{d}t^2$ have opposite signs; when it is not the case, we assume a nominal period of 70 yr. From the assumption that $\hat{\varphi}(t)$ extends back in time, and for a given choice of τ, we build an analytical solution for $\alpha(t)$ that obeys Eq. (S1). The initial condition $\alpha(t_{\rm o})$ is then taken from this analytical solution evaluated at $t_{\rm o}$, and is given by

$$\alpha(t_{\rm o}) = \left(\frac{C\omega\tau}{1+\omega^2\tau^2}\right)\cos\gamma + \left(\frac{C\omega^2\tau^2}{1+\omega^2\tau^2}\right)\sin\gamma\,. \tag{S3}$$

4 Best-fit torque parameters

Extended Data Fig. 3 shows the posterior distributions of all accepted samples (blue) from our MCMC algorithm and the high probability samples (orange) for which the ΔLOD misfit $\chi < 0.2$ ms. The high probability samples account for approximately 5% of all accepted samples. The posterior distributions for the high probability samples are shown in Fig. 2.

5 Recovered time-history of α

Extended Data Fig. 4 shows the time-histories of the axial misalignment angle $\alpha(t)$ of the long equatorial axis of the ICB topography for the samples of torque parameters that provide the best fit ($\chi < 0.2$ ms) to the multidecadal ΔLOD, for the separate experiments of (a) EM and (b) topographic coupling. The gravitational torque that best fits the ΔLOD features a maximum positive α approximately at year 2000.

6 Correlation between torque parameters

Supplementary Fig. 1a–d shows the correlation between Γ, τ and K_{em}, when the CMB torque is caused by EM coupling. These highlight two different torque regimes. When K_{em} is smaller than approximately 1, the gravitational torque dominates and explains mostly by itself the multidecadal ΔLOD. In this regime, τ is typically smaller than 10 yr and the gravitational torque is directly proportional to the product $\Gamma\tau$ (Methods) which remains generally smaller than 10^{20} N m yr; an equivalent fit to the LOD is achieved by increasing Γ while reducing τ by the same proportion. When K_{em} is instead larger than 1, EM coupling provides a stronger resistance to the driving gravitational torque. In this regime, the product $\Gamma\tau$ is generally larger than 10^{20} N m yr and increases proportionally with K_{em}. The region of the parameter space that provides the best ΔLOD fit is at the junction of these two regimes.

Supplementary Fig. 1e–h shows the correlation when the CMB torque is caused by topographic coupling. We find the equivalent two torque regimes as in the EM coupling case. The gravitational torque dominates when K_{top} is smaller than approximately 0.25, while the topographic torque counteracts the gravitational torque when K_{top} is greater than ~ 0.25. As for EM coupling, the region of the parameter space at the junction of the two regimes provides the best fit to the ΔLOD.

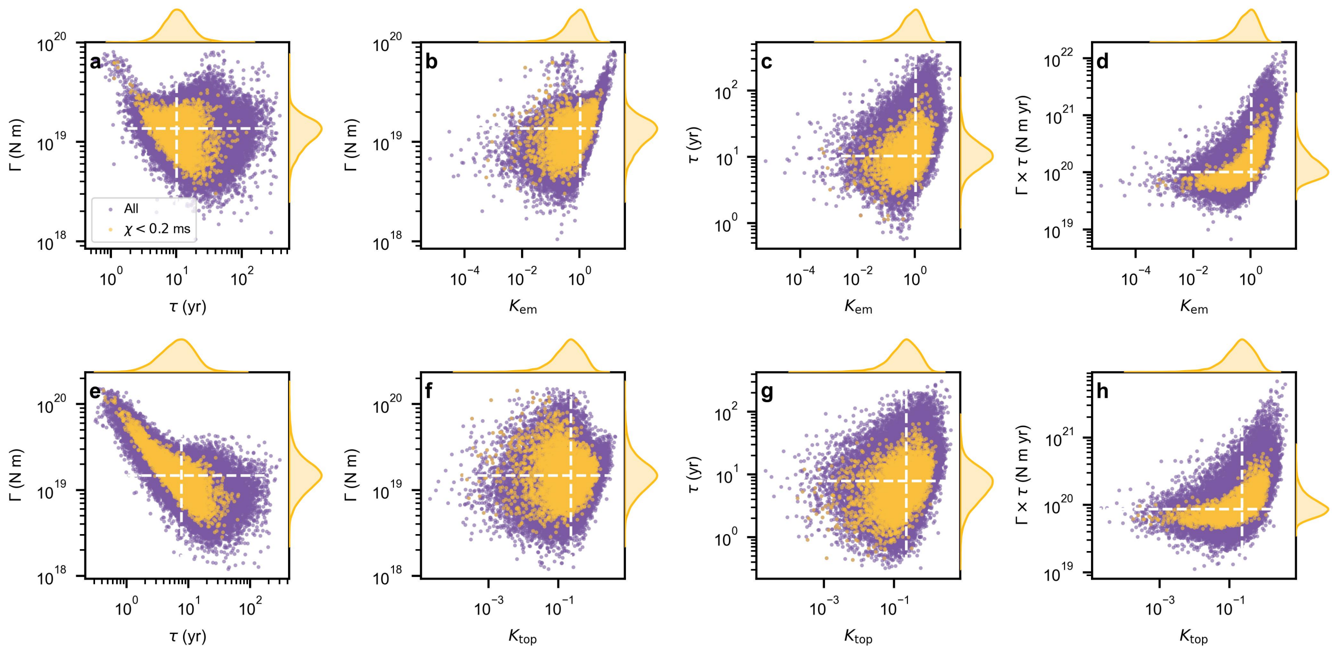

Supplementary Fig. 1: Correlation between the torque parameters. **a–d**, EM coupling scenario; **e–h**, Topographic coupling scenario. Purple dots: all samples; overlaid yellow dots: samples for which the ΔLOD misfit χ is < 0.2 ms. The posterior distributions of the torque parameters for these best-fit samples is shown on the top and right axes of each panel. The dotted white lines indicate the maximum a posteriori estimates of the distributions.

7 Diagnostic Tests of our MCMC algorithm

A key issue when using Markov Chain Monte Carlo (MCMC) methods is to determine when convergence has been reached and sampling can be stopped. Our results are based on five independent chains initialized from different starting points (Supplementary Table 2). The convergence of the posterior distributions based on these chains is evaluated with the Python package ArviZ (https://python.arviz.org/), by examining trace plots (Supplementary Fig. 2) and calculating the Gelman-Rubin statistic ($\hat{R}$[8,9]) and the effective sample size (ESS[10,11]).

Multi-chains of a parameter are considered to have converged when its $\hat{R}$ value falls below 1.005 and its ESS exceeds 15% of the total number of samples. The $\hat{R}$ values of Γ, τ and $K_{\rm em}$ of our five chains for EM coupling shown in Supplementary Fig. 2 are (1.000, 1.001, 1.001), and their ESS values are (34685, 30449, 44429). The $\hat{R}$ and ESS values of Γ, τ and $K_{\rm top}$ of our five chains for topographic coupling are (1.003, 1.002, 1.000) and (27584, 27400, 63825), respectively. The lowest ESS exceed 30% of the total number of retained samples (27400/48000 $\approx$ 30%). For each torque parameter, the posterior distributions from individual chains are very similar to one another (Supplementary Fig. 2), providing a visual check that the chains have converged. It is worth mentioning that the use of a covariance matrix in MCMC methods helps to improve the efficiency of the sampling and, in principle, does not affect the target distribution.

Supplementary Table 2: Starting samples and diagnostics of the five independent MCMC chains from which our results are derived, for the separate experiments of EM and topographic (TOP) coupling. The correlation coefficients and standard deviations of the covariance matrices, the step sizes and acceptance rates are those that apply at the end of the burn-in period, and are kept constant for subsequent samples. The initial covariance matrix is $\mathbf{\Sigma}_{ii} = (\sigma_\Gamma^2, \sigma_\tau^2, \sigma_{K_{cmb}}^2) = (10^{40}, 10^4, 1)$, where $i = 1, 2, 3$.

EM	First pick sample			Correlation coefficient			Standard deviation			step size	Acceptance rate
Chains	Γ_1	τ_1	$K_{\rm em}$	$\rho_{\Gamma\tau}$	$\rho_{\Gamma K_{\rm em}}$	$\rho_{\tau K_{\rm em}}$	σ_Γ	σ_τ	$\sigma_{K_{\rm em}}$	s	α_a
A1	1.99×10^{19}	36.3	4.41	0.02	0.79	0.31	5.61×10^{18}	25.6	1.23	0.31	0.073
B1	2.57×10^{19}	25.3	6.45	-0.01	0.82	0.27	5.75×10^{18}	18.3	1.29	0.54	0.050
C1	2.08×10^{19}	34.9	5.91	0.13	0.66	0.52	4.74×10^{18}	18.6	1.23	0.60	0.061
D1	1.64×10^{18}	29.0	0.57	-0.01	0.81	0.22	4.92×10^{18}	21.8	1.08	0.51	0.034
E1	1.41×10^{19}	54.2	0.39	-0.05	0.76	0.24	5.24×10^{18}	22.5	1.05	0.54	0.058
TOP	First pick sample			Correlation coefficient			Standard deviation			step size	Acceptance rate
Chains	Γ_1	τ_1	$K_{\rm top}$	$\rho_{\Gamma\tau}$	$\rho_{\Gamma K_{\rm top}}$	$\rho_{\tau K_{\rm top}}$	σ_Γ	σ_τ	$\sigma_{K_{\rm top}}$	s	α_a
A2	5.62×10^{18}	29.9	0.18	-0.49	0.14	0.17	7.16×10^{18}	11.4	0.29	0.88	0.059
B2	3.51×10^{19}	1.3	0.03	-0.46	0.03	0.28	8.04×10^{18}	12.1	0.31	0.71	0.060
C2	3.13×10^{18}	131.9	0.21	-0.40	0.09	0.17	9.92×10^{18}	13.0	0.30	0.80	0.042
D2	1.75×10^{19}	36.0	0.34	-0.40	0.30	0.17	5.61×10^{18}	15.9	0.30	0.70	0.057
E2	8.13×10^{18}	138.0	0.71	-0.44	0.11	0.18	7.49×10^{18}	14.2	0.30	0.67	0.063

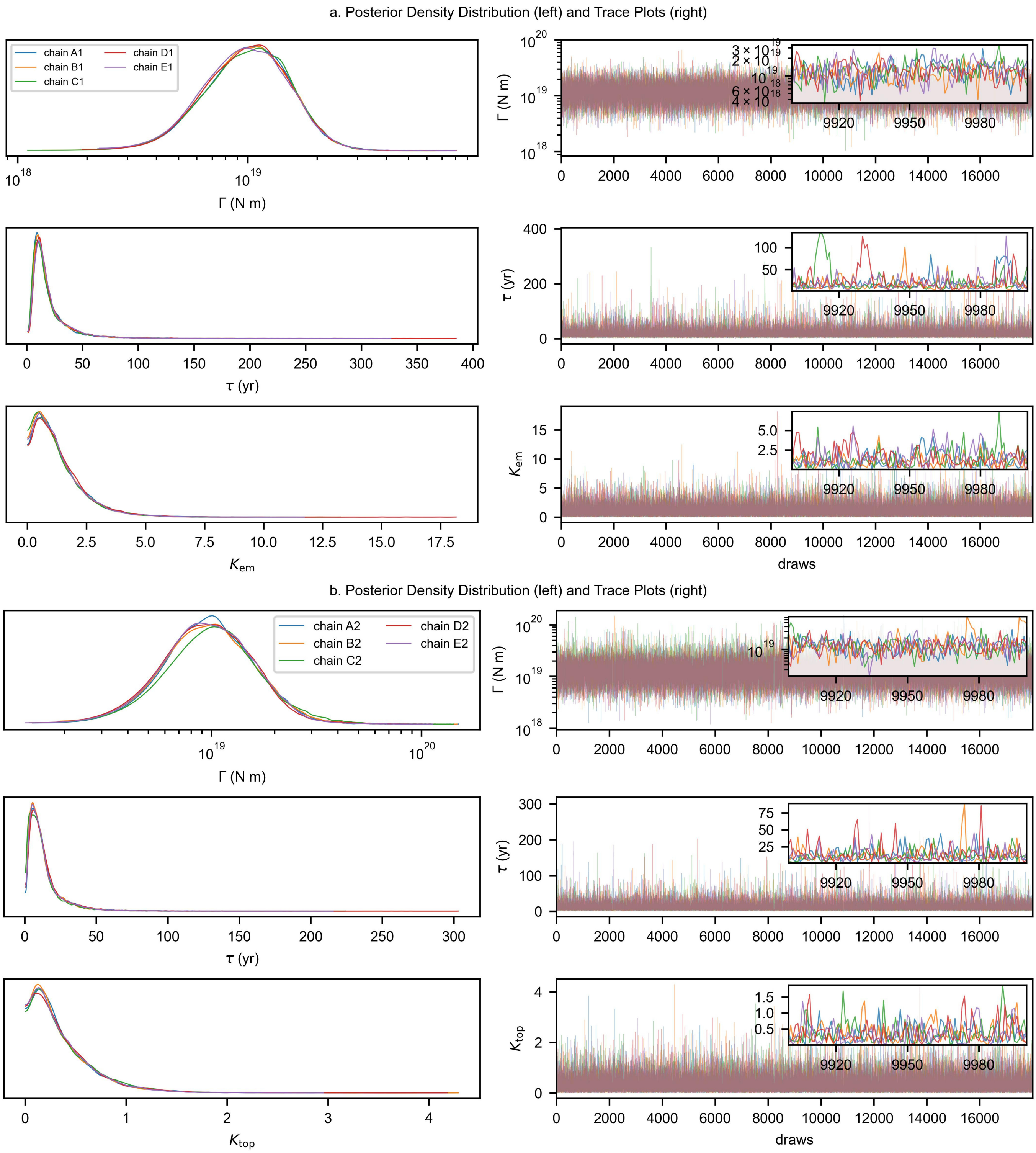

Supplementary Fig. 2: Convergence diagnostic tests for the five MCMC chains from which our results are derived, for the separate experiments of (**a**) EM coupling and (**b**) topographic coupling. Left column shows the posterior distributions of the torque parameters of each individual chains. Right column shows the trace plots for the torque parameters of each individual chains, with insets showing a blow up of a sequence of 100 samples.

8 Sensitivity tests for different inner core rotation histories

Our results depend on the model of inner core rotation history from ref.[7]. The longitudinal angle of axial angular rotation of the bulk of the inner core $\varphi(t)$ from this model is not measured directly but inferred from a model of the seismic velocity gradient within the inner core which remains uncertain. Here, we perform tests to determine how sensitive the torque parameters Γ, τ and $K_{\rm em}$ are to this adopted history. As the time-histories of the EM and topographic torques are broadly similar, we restrict these tests to the case when the CMB torque is caused by EM coupling.

To carry these tests, we approximate the model of $\varphi(t)$ from ref.[7] based on two separate analytical functions, before and after $t_m = 2001$, of the form

$$\varphi(t) = \bar{\varphi}_1 + \varphi_a \sin\left(\omega_1(t - t_{01})\right) , \qquad 1964 \leq t \leq t_m , \tag{S4a}$$
$$\varphi(t) = \bar{\varphi}_2 + \gamma(t - t_{02}) - c\,\varphi_a \sin\left(\omega_2(t - t_{02})\right) , \qquad t_m \leq t \leq 2021 , \tag{S4b}$$

where $\omega_1 = 2\pi/T_1$, $\omega_2 = 2\pi/T_2$, with periods $T_1 = 86\,$yr and $T_2 = 24\,$yr, reference phase times $t_{01} = 1992$ and $t_{02} = 2014.5$, amplitudes $\varphi_a = 2.35\,^\circ$ and $c\,\varphi_a$ where $c = 0.16$. The constant $\bar{\varphi}_2$ and slope γ are determined so that $\varphi(t)$ and $d\varphi(t)/dt$ are continuous at $t = t_m$,

$$\gamma = \varphi_a\omega_1 \cos\left(\omega_1(t_m - t_{01})\right) + c\,\varphi_a\omega_2 \cos\left(\omega_2(t_m - t_{02})\right) , \tag{S5a}$$
$$\bar{\varphi}_2 = \bar{\varphi}_1 - \gamma(t_m - t_{02}) + \varphi_a \sin\left(\omega_1(t_m - t_{01})\right) + c\,\varphi_a \sin\left(\omega_2(t_m - t_{02})\right) . \tag{S5b}$$

This time-history depends on a mean offset angle $\bar{\varphi}_1$ but its numerical value does not enter our model as the computation of the misalignment angle α involves the time derivative of φ (see Eq. (S1)). Supplementary Fig. 3 shows how this simple sinusoidal model compares with the model of ref.[7].

We assign a Gaussian error with standard deviation σ_φ on the amplitude φ_a and a common Gaussian error $\sigma_t = 0.5\,$yr on the reference times t_{01}, t_{02} and t_m; the latter results in a shift of $\varphi(t)$ forward or backward in time. We conduct five different experiments in which we vary the amplitude φ_a and shift forward or backward in time the reference times. In all these experiments, we keep $T_1 = 86\,$yr and $T_2 = 24\,$yr. For each experiment, we build posterior probability distributions for Γ, τ and $K_{\rm em}$ with the same MCMC procedure as outlined in the main text.

Case A is our reference scenario; we use an amplitude of $2.35\,^\circ$ with a standard deviation of $\sigma_\phi = 0.2\,^\circ$ and keep the original set of reference times ($t_{01} = 1992$, $t_{02} = 2014.5$ and $t_m = 2001$) to which we assign a common error of $\sigma_t = 0.5$. For cases B and C, we decrease and increase respectively the amplitude φ_a by a factor 2 while leaving the reference times unchanged. For cases D and E, we shift the time-history backward and forward in time, respectively, by 2 years, while keeping the reference φ_a. The choices of parameters for the different experiments are summarized in Supplementary Table 3.

The histograms showing the probability distributions of Γ, τ and $G = K_{\rm em} \cdot 10^8$ S for these five experiments are shown in Supplementary Fig. 4. The associated ΔLOD predictions and the time-histories of the gravitational and EM torques are shown in Supplementary Figs. 5 and 6, respectively. The time-histories of the bulk rotation angle φ and ICB misalignment angle α of cases B to E compared to case A, are shown in Supplementary Fig. 7. Supplementary Table 4 gives the 95% CI range of Γ, τ and $K_{\rm em}$ for all samples, and for samples that fit the observed ΔLOD to within a misfit $\chi < 0.2\,$ms.

Decreasing or increasing the amplitude φ_a by a factor 2 (cases B and C, respectively) does not change τ and G appreciably. However, the best-fit Γ values are shifted by a factor 2, inversely proportional to the change in the amplitude φ_a. This simply reflects that the amplitude of the gravitational torque required to explain the multidecadal ΔLOD involves the product of Γ and α, and the latter is proportional to φ (Supplementary Fig. 7a,b).

A shift in the inner core time-history backward (case D) or forward (case E) in time by 2 years, does not lead to a significant change in G. However, the shift in time of φ implies that a different value of τ is needed in order to optimize the phase of the gravitational torque (which always corresponds to a maximum α near year 2000, Supplementary Fig. 7c,d). With a backward time shift, maximizing α

near year 2000 requires less viscous relaxation (higher τ). Conversely, a forward shift in time requires more viscous relaxation (smaller τ). When $\tau \ll T_1$, the amplitude of the gravitational torque is directly proportional to the product $\Gamma\tau$ (see Methods), so the latter remains approximately constant. Hence, the higher τ for case D leads to a decrease in Γ, while the smaller τ for case E leads to an increase in Γ.

Overall, these tests reveal that G (or, equivalently, K_{em}) is not overly sensitive to small changes in the inner core time-history, that a shift in time of the latter alters τ but leaves the product of Γ and τ unchanged, and that the inferred range of Γ that we retrieve is inversely proportional to the assumed amplitude of the bulk differential rotation angle of the inner core.

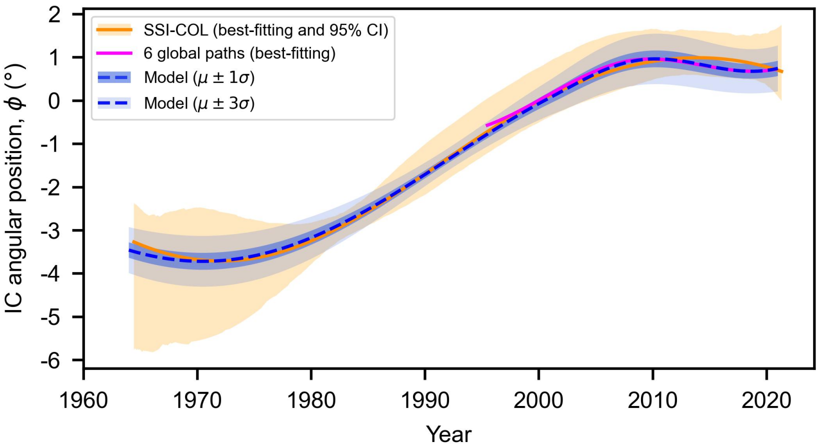

Supplementary Fig. 3: The time-history of the axial angular position of the inner core, $\varphi(t)$, from ref.[7] and from Eq. (S4). The magenta line corresponds to the reconstruction from ref.[7] between 1995–2021 based on 6 different seismic rays paths. The orange line corresponds to the reconstruction from ref.[7] between 1964–2021 based on the single seismic ray path between South Sandwich Island and College station (SSI-COL); the light orange envelope shows the 95% CI. The dash blue line shows the analytical fit of the seismic reconstruction based on Eq. (S4) with $\phi_a = 2.35\,°$, $t_{01} = 1992$, $t_{02} = 2014.5$ and $t_m = 2001$. The dark blue and light blue envelopes show the spread covered by one and three standard deviations, respectively, when taking into account the Gaussian errors σ_φ and σ_t.

Supplementary Table 3: Different scenarios of inner core differential rotation, with a common Gaussian error of $\sigma_t = 0.5\,\mathrm{yr}$ applied to the reference times t_{01}, t_{02} and t_m.

Case	ϕ_a (°)	t_{01} (yr)	t_{02} (yr)	t_m (yr)	T_1 (yr)	T_2 (yr)
A	$\mathcal{N}(2.35, 0.2^2)$	$\mathcal{N}(1992, \sigma_t^2)$	$\mathcal{N}(2014.5, \sigma_t^2)$	$\mathcal{N}(2001, \sigma_t^2)$	86	24
B	$\mathcal{N}(1.18, 0.1^2)$	$\mathcal{N}(1992, \sigma_t^2)$	$\mathcal{N}(2014.5, \sigma_t^2)$	$\mathcal{N}(2001, \sigma_t^2)$	86	24
C	$\mathcal{N}(4.70, 0.4^2)$	$\mathcal{N}(1992, \sigma_t^2)$	$\mathcal{N}(2014.5, \sigma_t^2)$	$\mathcal{N}(2001, \sigma_t^2)$	86	24
D	$\mathcal{N}(2.35, 0.2^2)$	$\mathcal{N}(1990, \sigma_t^2)$	$\mathcal{N}(2012.5, \sigma_t^2)$	$\mathcal{N}(1999, \sigma_t^2)$	86	24
E	$\mathcal{N}(2.35, 0.2^2)$	$\mathcal{N}(1994, \sigma_t^2)$	$\mathcal{N}(2016.5, \sigma_t^2)$	$\mathcal{N}(2003, \sigma_t^2)$	86	24

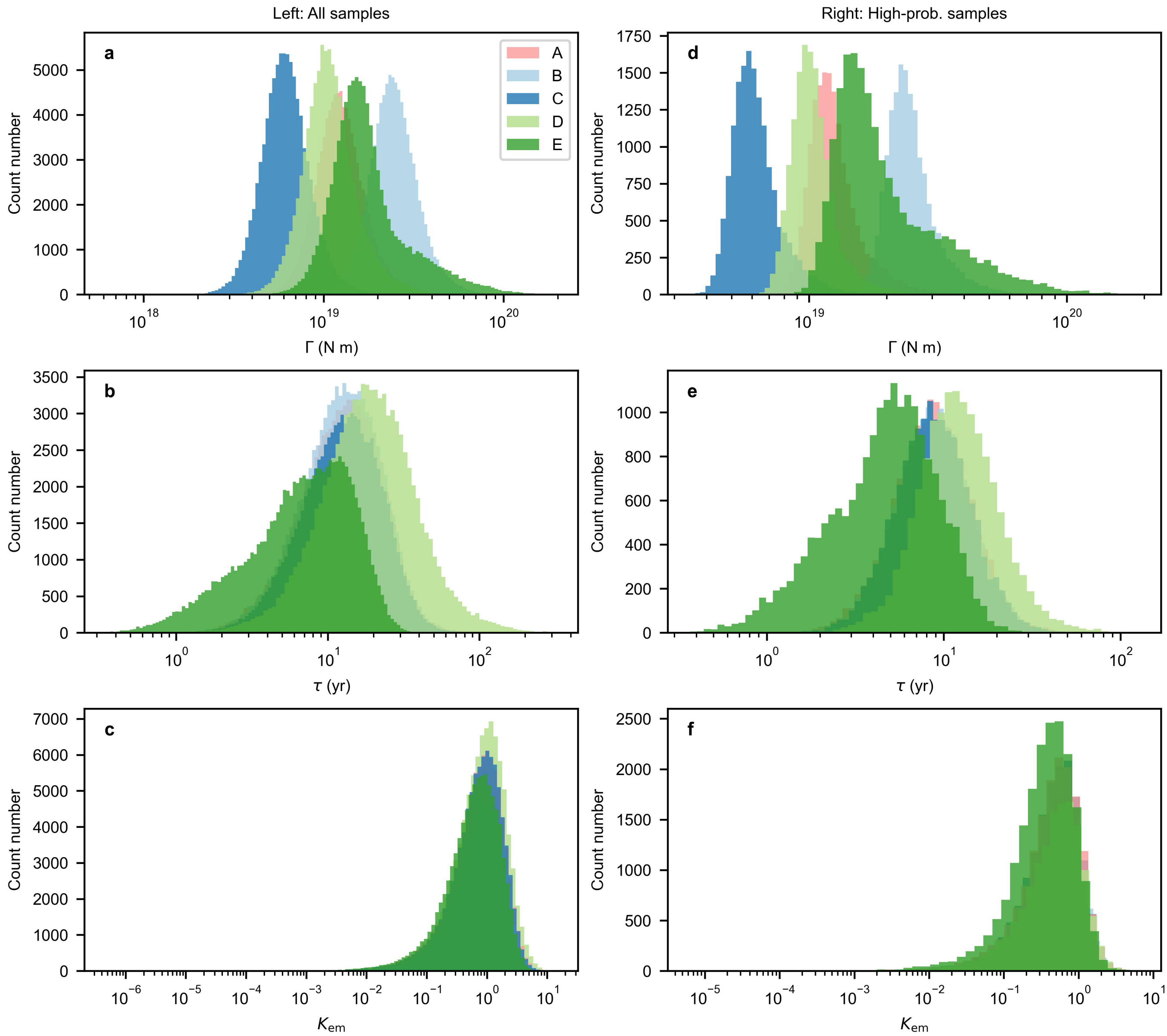

Supplementary Fig. 4: Posterior distributions of Γ, τ and K_{em} for the different inner core differential rotation scenarios. **a**–**c**, All samples from our MCMC method. **d**–**f**, High probability samples fitting the observed ΔLOD within a misfit $\chi < 0.2$ ms.

Supplementary Table 4: Recorded 95% CI range of Γ, τ and K_{em} for the different inner core differential rotation scenarios, for all samples and for the high probability samples fitting the observed ΔLOD within a misfit $\chi < 0.2$ ms. The values in parentheses indicate the maximum a posteriori estimates.

	All samples			**High Prob. Samples**		
Case	**Γ** (10^{19} N m)	$\boldsymbol{\tau}$ (yr)	$\boldsymbol{G}$ (10^7 S)	**Γ** (10^{19} N m)	$\boldsymbol{\tau}$ (yr)	$\boldsymbol{G}$ (10^7 S)
A	0.7–2.4	3.2–35.3	0.5–32.3	0.9–2.3 (1.2)	3.1–22.4 (8.8)	0.4–17.0 (5.8)
B	1.4–4.8	3.3–35.4	0.5–32.0	1.8–4.4 (2.3)	3.2–22.5 (8.5)	0.4–16.6 (6.1)
C	0.3–1.2	3.4–35.0	0.5–31.2	0.4–1.1 (0.6)	3.3–22.7 (8.3)	0.4–16.9 (6.4)
D	0.6–2.4	4.2–78.9	0.5–37.1	0.8–1.7 (1.0)	4.3–35.9 (11.6)	0.3–18.3 (6.5)
E	0.8–6.5	1.0–21.5	0.4–27.8	1.1–7.0 (1.5)	1.0–14.3 (5.3)	0.3–14.8 (4.8)

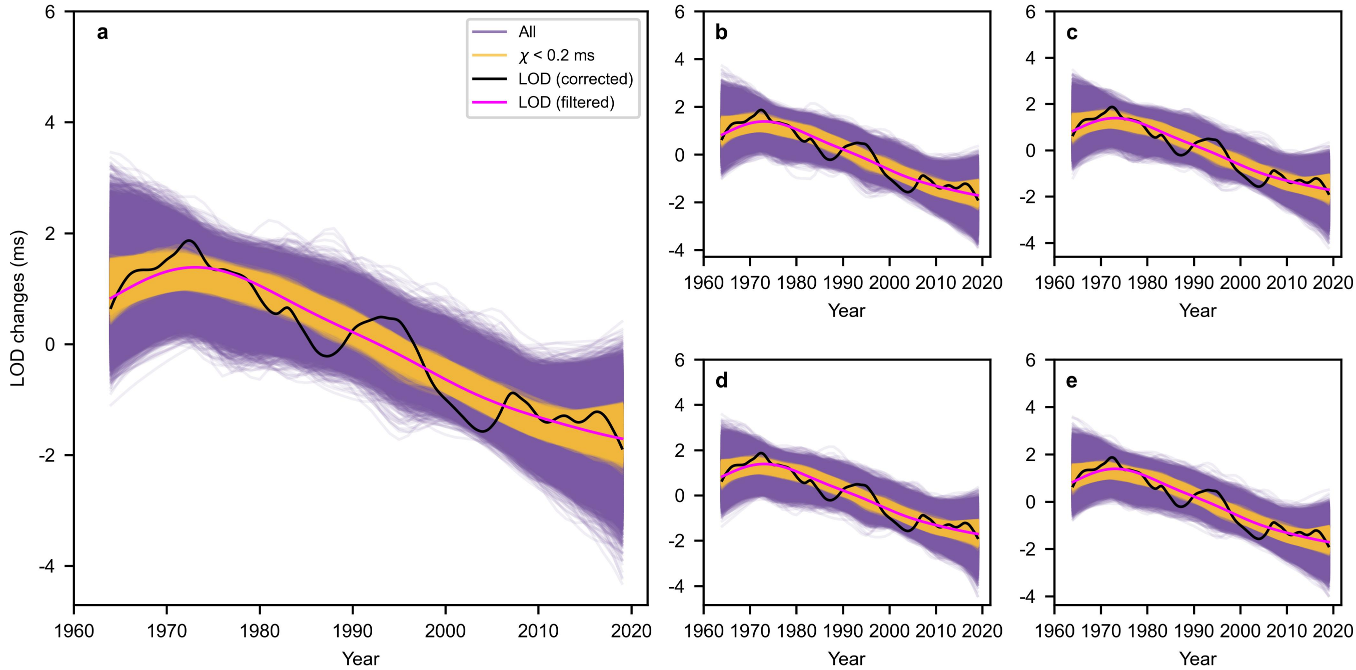

Supplementary Fig. 5: Predicted ΔLOD between 1964–2019 for the different inner core differential rotation scenarios. Panels **a** to **e** corresponds to cases A to E.

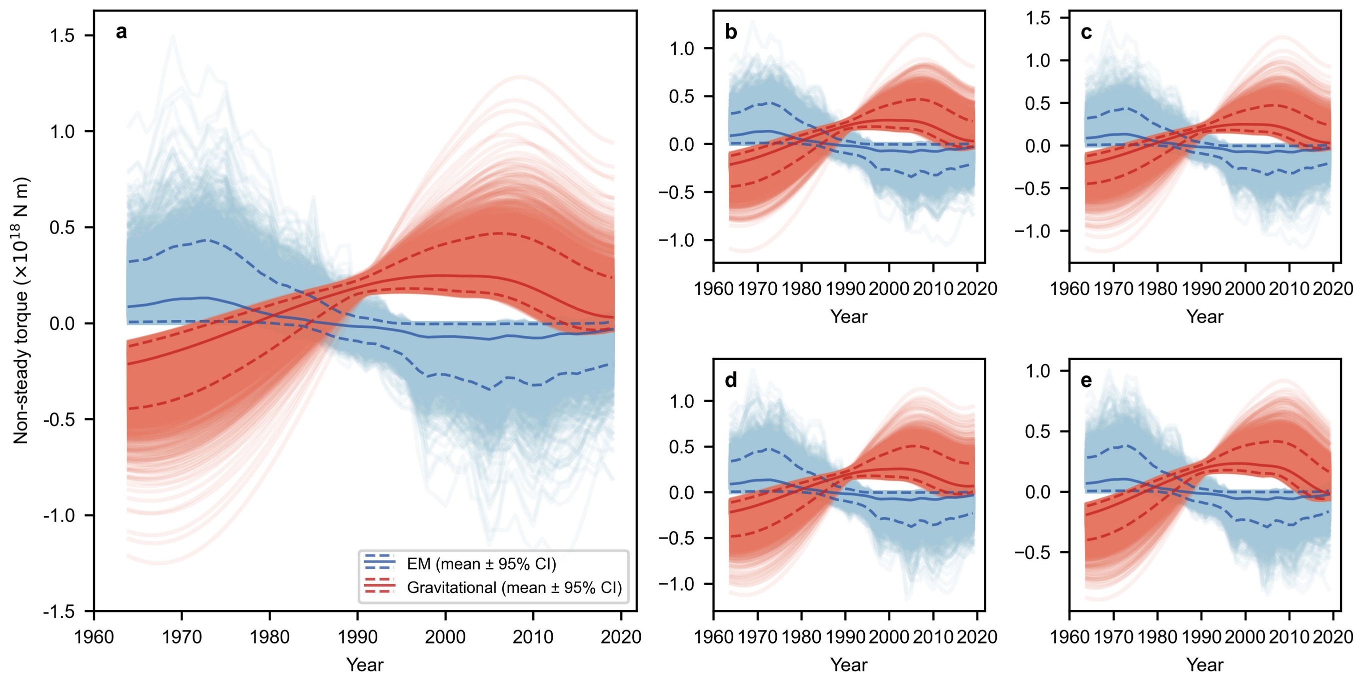

Supplementary Fig. 6: Predicted non-steady gravitational and EM torques for the different inner core differential rotation scenarios. Panels **a** to **e** corresponds to cases A to E. The median and 95% CI are shown for samples fitting the observed ΔLOD within a misfit $\chi < 0.2\,\text{ms}$.

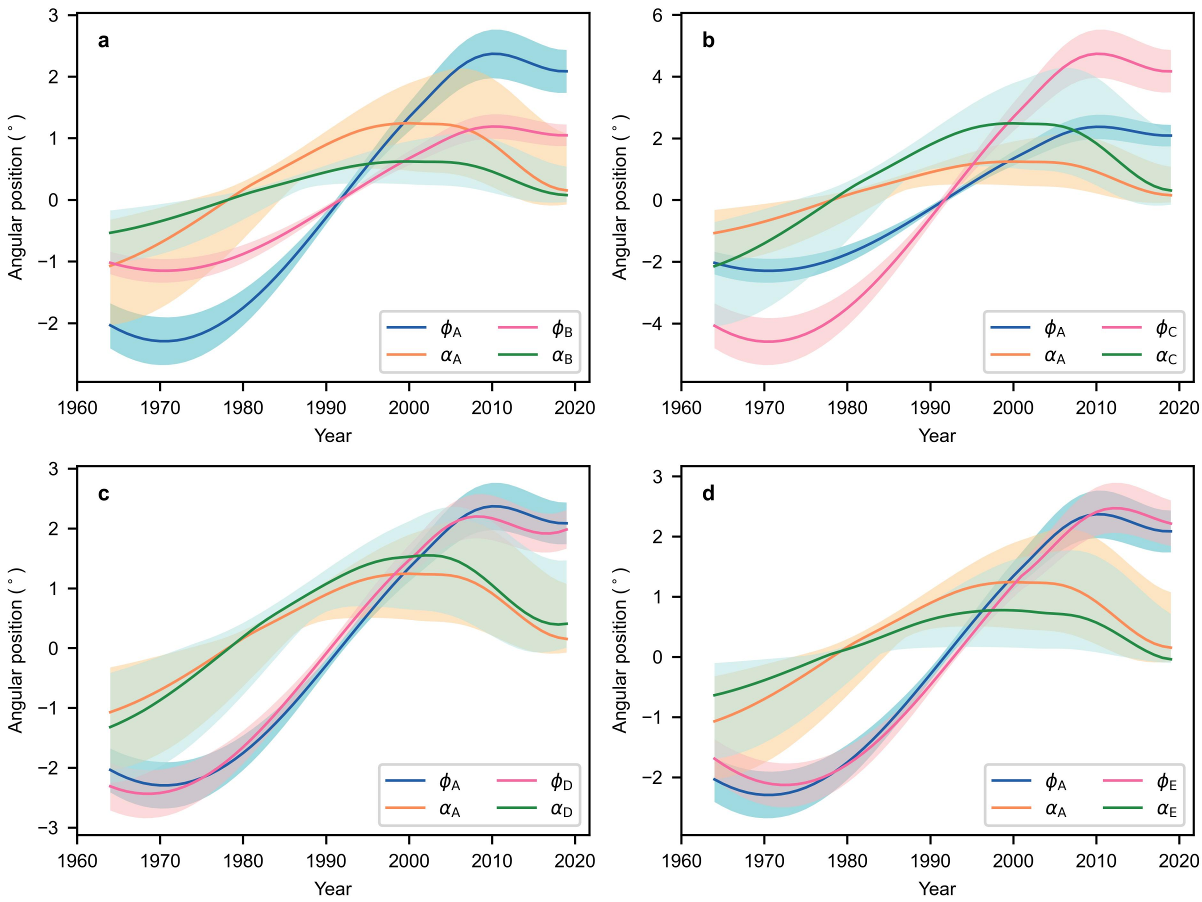

Supplementary Fig. 7: The bulk rotation φ and ICB misalignment angle α of scenarios B to E compared to the reference (case A) inner core differential rotation history. The solid line represents the median value and the shadow region highlights the 95% CI region from the high probability samples.

9 Sensitivity tests for different core flow models

To assess the sensitivity of our results to the chosen model of core flow, we consider two additional models which we label PNAS2022 (from ref.[12]) and GJI2019 (from ref.[13]). Supplementary Tables 5 (for EM coupling) and 6 (for topographic coupling) give the maximum a posteriori (MAP) estimates and 95% CI of the torque parameters from the high probability samples for each flow model compared with those from the flow model GJI2023 (from ref.[4]) that we used in our study. Supplementary Figs. 8 (for EM coupling) and 9 (for topographic coupling) show the posterior distributions.

The MAP estimates and 95% CI are very similar between the GJI2023 and PNAS2022 flow models, varying by no more than about 15%. Flow model GJI2019 gives slightly different results, although the difference with GJI2023 is never more than a factor of 2. These comparisons show that the exact values of the MAP and 95% CI of the torque parameters that we retrieve from our MCMC algorithm are sensitive to the choice of core flow models. Nevertheless, the torque parameters that we retrieve are robust in the sense that the MAP estimates do not generally change by more than 15-20% and the posterior distributions for different flow models overlap to a large degree.

Supplementary Table 5: The range of the 95% CI and maximum a posteriori (MAP) estimates of the torque parameters from different core flow models that provide the best fit to the multidecadal ΔLOD, when the CMB torque is caused by EM coupling ($K_{\mathrm{cmb}} = K_{\mathrm{em}}$).

	High-probability samples		
core flow model	$\boldsymbol{\Gamma}$ (10^{19} N m)	$\boldsymbol{\tau}$ (yr)	$\boldsymbol{K}_{\mathbf{em}}$
GJI2019	1.2 (0.5 $\sim$ 3.0)	12.3 (5.0 $\sim$ 60.3)	1.11 (0.08 $\sim$ 3.42)
PNAS2022	1.3 (0.6 $\sim$ 2.1)	10.0 (4.2 $\sim$ 34.3)	0.91 (0.05 $\sim$ 2.68)
this study (GJI2023)	1.4 (0.6 $\sim$ 2.2)	10.2 (4.1 $\sim$ 30.5)	1.08 (0.05 $\sim$ 2.89)

Supplementary Table 6: The range of the 95% CI and maximum a posteriori (MAP) estimates of the torque parameters from different core flow models that provide the best fit to the multidecadal ΔLOD, when the CMB torque is caused by topographic coupling ($K_{\mathrm{cmb}} = K_{\mathrm{top}}$).

	High-probability samples		
core flow model	$\boldsymbol{\Gamma}$ (10^{19} N m)	$\boldsymbol{\tau}$ (yr)	$\boldsymbol{K}_{\mathbf{top}}$
GJI2019	1.1 (0.5 $\sim$ 2.0)	10.6 (3.7 $\sim$ 33.3)	0.40 (0.03 $\sim$ 0.96)
PNAS2022	1.7 (0.6 $\sim$ 4.3)	5.0 (1.6 $\sim$ 18.9)	0.24 (0.01 $\sim$ 0.81)
this study (GJI2023)	1.5 (0.6 $\sim$ 4.2)	7.8 (1.7 $\sim$ 21.5)	0.23 (0.01 $\sim$ 0.83)

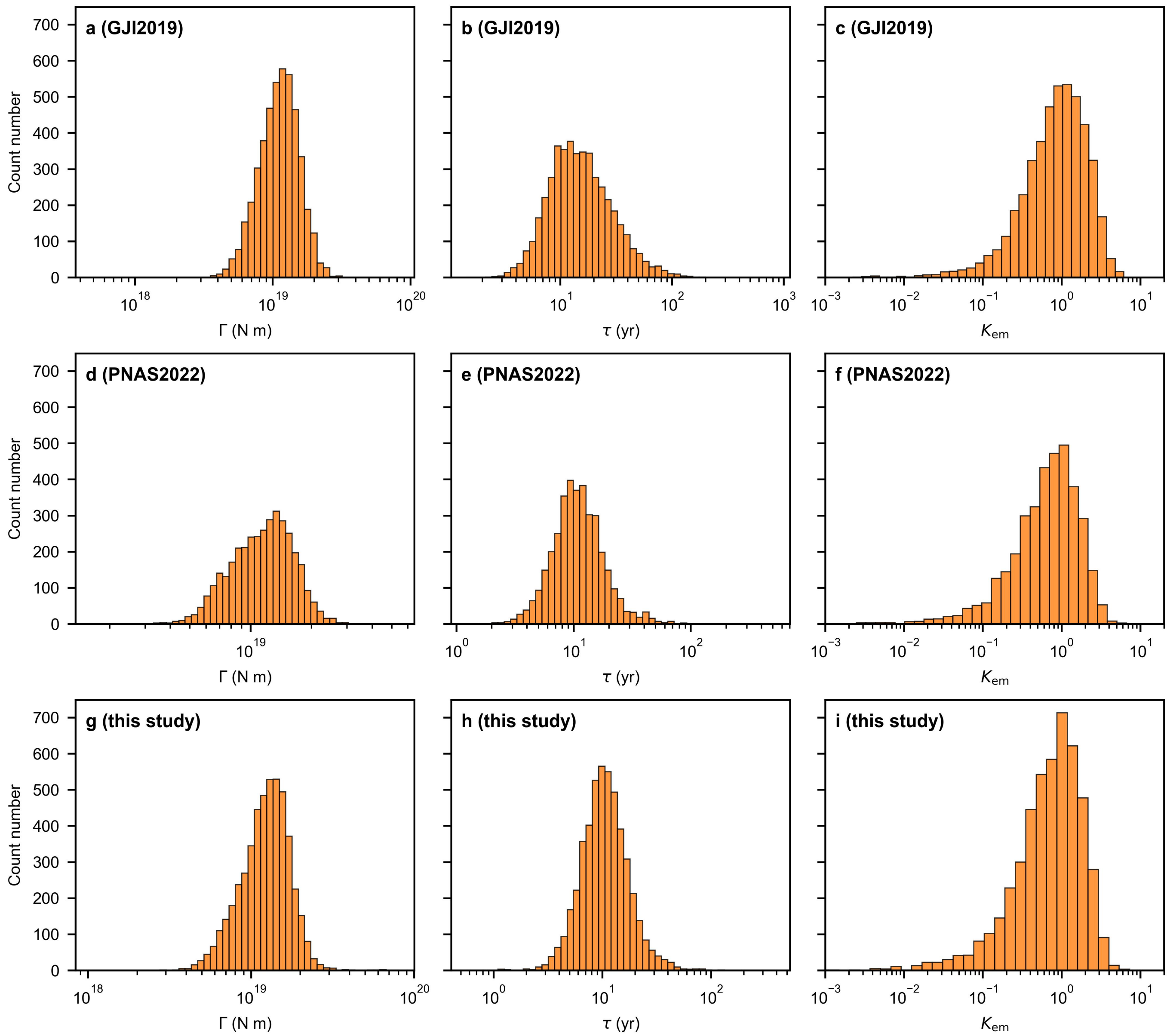

Supplementary Fig. 8: Posterior distributions of the torque parameters $(\Gamma, \tau, K_{\mathrm{em}})$ from the high probability samples of different core flow models when the CMB torque is from EM coupling. **a**–**c**, core flow model GJI2019 (ref.[13]); **d**–**f**, core flow model PNAS2022 (ref.[12]). **g**–**i**, core flow model GJI2023 (ref.[4]) used for the results shown in the main text.

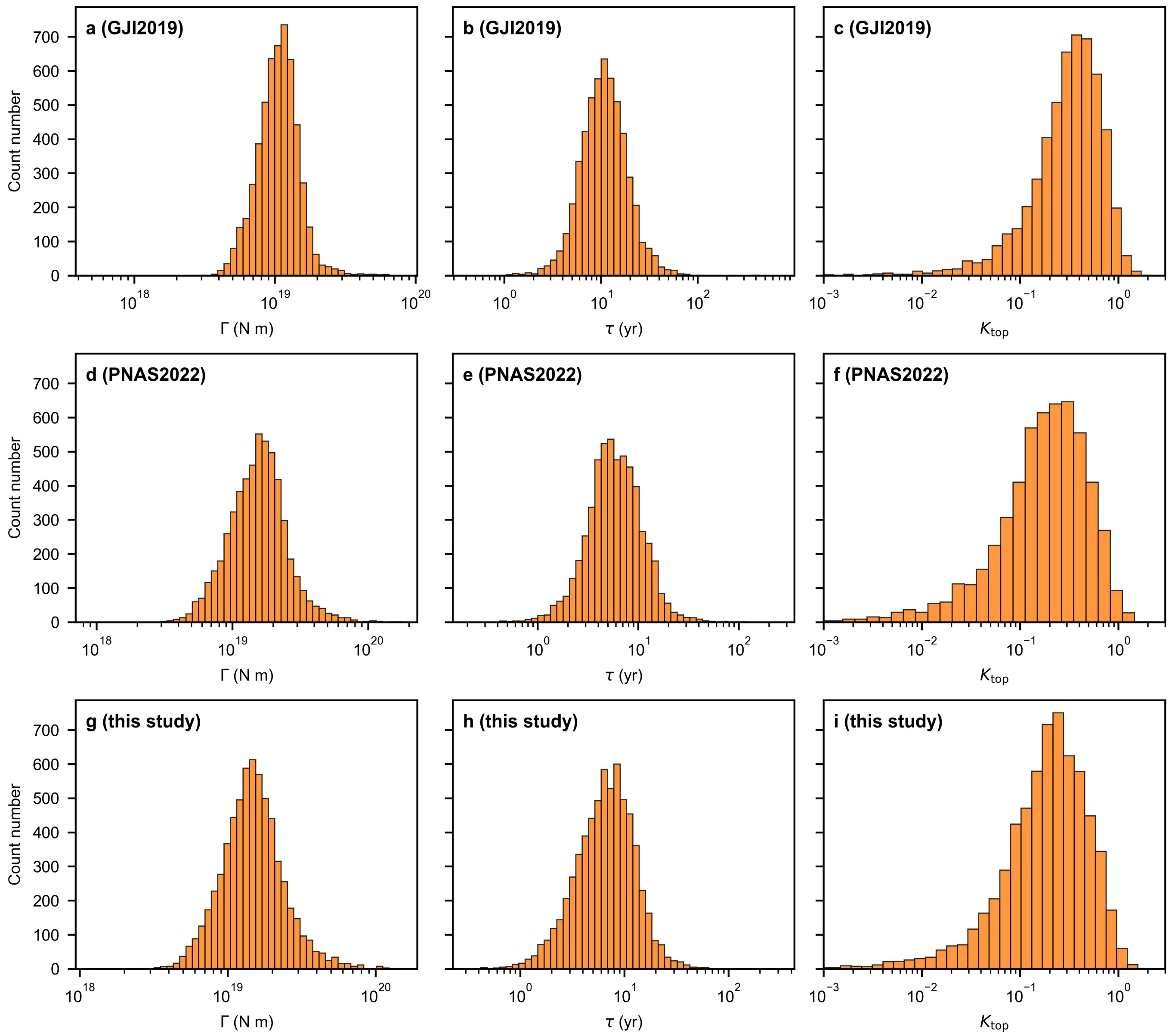

Supplementary Fig. 9: Posterior distributions of the torque parameters ($\Gamma, \tau, K_{\mathrm{top}}$) from the high probability samples of different core flow models when the CMB torque is from topographic coupling. **a**–**c**, core flow model GJI2019 (ref.[13]); **d**–**f**, core flow model PNAS2022 (ref.[12]). **g**–**i**, core flow model GJI2023 (ref.[4]) used for the results shown in the main text.

10 Multidecadal core flow changes between 1950 and 2019

Supplementary Fig. 10 shows the temporal variations of the zonal (axisymmetric) azimuthal flow (v_ϕ) at the CMB at different latitudes between 1950 and 2019 for the ensemble solution of the core flow model from ref.[4]. The time-average zonal flow at each latitude between 1950–2019 has been removed. In the region outside the tangent cylinder (TC), v_ϕ is broadly more eastward between 1950 and 1984, and broadly more westward between 1985 and 2019 (see Fig. 4a). Although the variations of v_ϕ (both versus latitude and time) are admittedly more complex, this simple first order picture of the multidecadal v_ϕ outside the TC is consistent with a CMB torque that is broadly eastward in 1950–1984 then westward in 1985–2019, and consistent with the basic flow cartoons shown in Fig. 4b,c.

Inside the TC, the multidecadal v_ϕ is more complex. This region covers a small surface area of the CMB so the flow within it may not be as well recovered. The v_ϕ flows in the North and South hemispheres are markedly different. Larger temporal variations occur inside the Northern part of the

TC, where v_ϕ has been more westward near 1960 and more eastward near 2005 compared to its average (see Fig. 4a). If these v_ϕ changes at the CMB are reflective of the v_ϕ near the ICB (as it would be the case for axially invariant flows), such flows should entrain (via EM torque at the ICB) a westward angular velocity of the inner core Ω_i near 1960 and an eastward Ω_i near 2005. Ω_i is related to the bulk axial angular position of the inner core φ by $\frac{d\varphi}{dt} = \Omega_\mathrm{i}$. If the viscous relaxation time τ of the inner core is short (a few years), then the misalignment angle α of the ICB topography is approximately equal to $\alpha \approx \tau \frac{d\varphi}{dt} \approx \tau \, \Omega_\mathrm{i}$ (see Methods). This implies that α should be negative (westward of its equilibrium point) near 1960 and positive (eastward of its equilibrium point) near 2005. This is consistent with a gravitational torque on the mantle that is more westward than on average in the decades around 1960, and more eastward than on average in the decades around 2000, as we find in our results, and as shown in the cartoons of Fig. 4b,c.

To complement Fig. 4a, Supplementary Fig. 11 shows the angular velocity $\Omega_\mathrm{f} = v_\phi/s$ as a function of latitude, where s is cylindrical radius, for the same epochs. This further illustrates that the mean rotation outside the TC is eastward in the 35 years centered on 1967 and westward in the 35 years centered on 2002. The mean angular velocity inside the TC is broadly opposite: it is westward around 1967 and eastward around 2002, although this mainly reflects the flow in the Northern part. Note that the time-averaged flow between 1985–2019 is almost a perfect mirror image of the time-average flow between 1950–1984.

We also show in Supplementary Fig. 11 the prediction of the angular velocity of the inner core $\Omega_\mathrm{i} = \frac{d\varphi}{dt}$ based on our analytical function of φ (Eq. (S4) above) for the same time snapshots and time intervals (and assuming that the periodic function extends before 1964). Ω_i is in the same direction and of the same order of magnitude as the angular velocity of the zonal core flow inside the TC, as we expect if zonal flows are axially invariant and for a strong EM coupling at the ICB. The similar amplitudes of the angular velocity of the flow inside the TC and the differential inner core rotation inferred from seismic observations of ref.[7] provide further support that the latter is geophysically reasonable.

Overall, the broad $\sim$70-yr oscillation of v_ϕ at the CMB between 1950 and 2019 is captured, in its simplest form, by an oscillation between the regions inside and outside the TC, as depicted by the simple cartoons shown in Fig. 4b,c.

Further complementing Fig. 4a, Extended Data Fig. 5 shows v_ϕ as a function of latitude at the individual epochs of 1967 and 2002 (panel a) and its time average over 1950–1984 and over 1985–2019 (panel b). Here, we also show v_ϕ in 1932 (panel a) and its time average over 1915–1949. Some similarities exist between the flow structures in 1985–2019 and 1915–1949: both flows are eastward near the equator. However, there are some important differences too: the 1915–1949 flow is not dominantly eastward outside the TC, and the strongest westward flow inside the TC occurs in the South hemisphere. The flow pattern in 1915–1949 is not a repeated image of the flow in 1985–2019, suggesting that the $\sim$70-yr oscillation that characterizes the time-window 1950–2019 is not a simple, repeating periodic pattern.

Admittedly, the quality of the flow degrades the further we go back in time as the quality of the magnetic field data becomes less reliable. As such, it is difficult to draw firm conclusions on whether the $\sim$70-yr oscillation that we have identified extends further back in time. Nevertheless, the flow in 1915–1949 does not suggest that it does. The complex variations of v_ϕ inside the TC hint that, in general, the time-history of the gravitational torque is more complex than a simple $\sim$70-yr oscillation, and not necessarily always approximately equal and opposite to the CMB torque, even though this simplified picture applies over the past 7 decades.

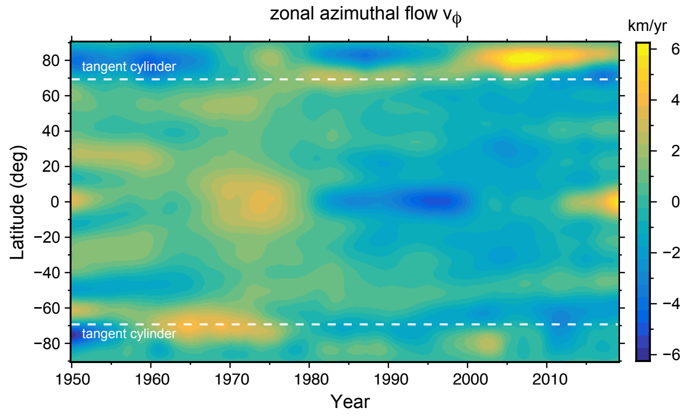

Supplementary Fig. 10: Differential zonal azimuthal flow (color bar, in km/yr) at the CMB versus latitude and time from the ensemble solution of the core flow model from ref.[4]. The time-averaged zonal flow at each latitude between 1950–2019 has been removed.

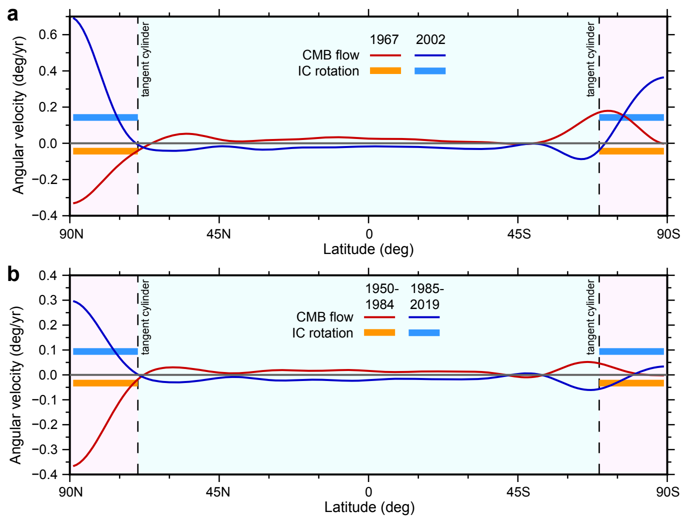

Supplementary Fig. 11: Angular velocity of zonal core flow versus latitude at the CMB. **a**, Flow in 1967 (red line) and 2002 (blue line); **b**, Mean flow between 1950–1984 (red line) and 1985–2019 (blue line). In each panel, the thick orange and thick light blue lines show the angular velocities $\Omega_\mathrm{i} = d\varphi/dt$ of the inner core based on φ from Eq. (S4) over the same time snapshots and time intervals. Pink highlights the regions inside the tangent cylinder; cyan highlights the region outside the tangent cylinder.

11 Constraints on the buoyancy frequency from the topographic torque

We write the axial component of the topographic torque as (Eq. (12) of Methods)

$$\Gamma_\mathrm{top} = K_\mathrm{top}\mathcal{D}_\mathrm{ref}\, r_\mathrm{c} \oint_\mathrm{CMB} F(\theta)\,\mathrm{sign}(v_\phi)\sqrt{\|v_\phi\|}\,\sin\theta\,\mathrm{d}S\,. \tag{S6}$$

The function $F(\theta)$ accounts for the projection of the Coriolis force in the direction normal to the local boundary. It is given approximately by[14]

$$F(\theta) \approx \begin{cases} 0.65 + 0.05\exp\left(-\frac{(\theta-\pi/3)^2}{\varsigma^2}\right) - 0.65\exp\left(-\frac{(\theta-\pi/2)^2}{\zeta^2}\right), & 0 \le \theta \le \pi/2 \\ 0.65 + 0.05\exp\left(-\frac{(2\pi/3-\theta)^2}{\varsigma^2}\right) - 0.65\exp\left(-\frac{(\pi/2-\theta)^2}{\zeta^2}\right), & \pi/2 < \theta \le \pi \end{cases}, \tag{S7}$$

where $\varsigma = 0.303$ and $\zeta = 0.180$, and is shown in Extended Data Fig. 9. The modulation of the torque by $F(\theta)$ implies that the dominant contribution to the tangential stress is caused by flow at mid- to high-latitudes at the CMB.

For a given core flow model, the amplitude of the torque is determined by $\mathcal{D} = K_{\text{top}}\mathcal{D}_{\text{ref}}$, where K_{top} is a dimensionless parameter and $\mathcal{D}_{\text{ref}}$ is a reference value set equal to $1\,\text{kg}\,\text{m}^{-3/2}\,\text{s}^{-3/2}$. $\mathcal{D}$ is connected to the buoyancy frequency N, the magnetic field strength B_0 and the wavelength ℓ and amplitude h of the CMB topography by

$$K_{\text{top}}\mathcal{D}_{\text{ref}} = \mathcal{D} = \rho\Omega_{\text{o}}\frac{\sqrt{\rho\mu\eta}}{B_0}\frac{Nh^2}{\sqrt{\ell}}, \tag{S8}$$

where ρ is the fluid density, η is the magnetic diffusivity, $\mu = 4\pi \times 10^{-7}\,\text{H/m}$ is the magnetic permeability of free space, and $\Omega_{\text{o}} = 7.29 \times 10^{-5}\,\text{s}^{-1}$ is Earth's mean rotation rate.

Typical values near the top of the core are $\rho = 10^4\,\text{kg}\,\text{m}^{-3}$, $\eta = 0.8\,\text{m}^2/\text{s}$, and a magnetic field strength $B_0 = 5 \times 10^4\,\text{T}$. Based on these, we can express the buoyancy frequency, normalized by Ω_{o} as

$$\frac{N}{\Omega_{\text{o}}} \approx 94\,\frac{\sqrt{\ell}}{h^2}\,K_{\text{top}}\,, \tag{S9}$$

when ℓ and h are in units of meters. For adopted choices of h and ℓ, we can thus compute the normalized buoyancy frequency that matches specific values of K_{top}. Supplementary Fig. 12 shows N/Ω_{o} as a function of ℓ and h for $K_{\text{top}} = 0.83$ and $K_{\text{top}} = 0.23$, respectively, the upper bound and maximum a posteriori estimate of K_{top} from our Bayesian inversion. As an example on how to interpret these results, for a representative topography height of $h = 1\,\text{km}$ and wavelength $\ell = 10^4\,\text{km}$, $K_{\text{top}} = 0.83$ implies that $N/\Omega_{\text{o}} \approx 0.25$, and $K_{\text{top}} = 0.23$ gives $N/\Omega_{\text{o}} \approx 0.07$.

The topographic torque model assumes a uniform stratification, which may not be appropriate for Earth as N may vary both as a function of radius and geographic location. Hence, while Supplementary Fig. 12 may provide a general guide for how N/Ω_{o} maps as a function of ℓ and h, it may not be precise. Furthermore, the difficulty in interpreting the results of Supplementary Fig. 12 is to choose which set of ℓ and h values are the most representative. The topographic torque model assumes a steady-state equilibrium and a periodic topography that extends to infinity in the horizontal direction; it is devised to capture the stress caused by a large scale flow v_ϕ which appears approximately uniform when compared to the scale of the shorter localized wavelength ℓ of the CMB topography. As such, smaller choices of ℓ are more consistent with the torque model. However, the net torque results from the effect caused by all wavelengths, and since h increases with ℓ, longer wavelengths contribute proportionally more to the torque.

To guide our interpretation, we include in Supplementary Fig. 12 the rms of h at different spherical harmonic degrees (converted to ℓ) for a selected set of CMB topography models from ref. [15]. The amplitude of the topography h generally increases with the wavelength ℓ. Let us consider model SBF2012-TG[16] as an example, a model obtained from a joint inversion of seismic body waves and the dynamic CMB topography induced by viscous mantle flow. At spherical harmonic degree 12 ($\ell \sim 2000\,\text{km}$), $h \sim 200\,\text{m}$, and this gives $N/\Omega_{\text{o}} \sim 3$ for $K_{\text{top}} = 0.83$ and $N/\Omega_{\text{o}} \sim 1$ for $K_{\text{top}} = 0.23$. However, the larger topography $h \sim 1\,\text{km}$ at an intermediate wavelength of $\ell \sim 5000\,\text{km}$ restricts N/Ω_{o} to be well below 1. Model SBF2012-TGppv[16] is based on a similar joint inversion, but with a viscosity of the lower 250 km of the mantle reduced by a factor 10^3 to account for the reduced viscosity of the postperovkite (pPv) phase[17]. This results in a much reduced dynamic CMB topography, smaller by approximately a factor 10 compared to the typical amplitude predicted by other models. Such a low CMB topography would permit larger values of N/Ω_{o}. However, the pPv phase should be confined to lenses in cold, downwelling regions of the lower mantle[18,19], not be present in the whole of the D" region. In mantle convection models that include the pPv phase change, its lower viscosity results in a smaller CMB topography amplitude, but only by a factor of approximately 2 (ref. [20]).

Hence, it is difficult to extract a precise value of N/Ω_{o} based on our results, both because of the uncertainty of the CMB topography and because it is unclear which wavelength ℓ is the most appropriate for the topographic coupling model. Nevertheless, using a representative CMB topography of a few hundred meters at a wavelength of a few thousand kilometers, consistent with the ensemble of CMB topography models, limits N/Ω_o to be smaller than 1. Although crude, this upper bound is also generous, as it assumes that the CMB torque is entirely caused by topographic coupling. If a significant portion of the CMB torque is caused instead by EM coupling, then the upper limit on N/Ω_o is further reduced.

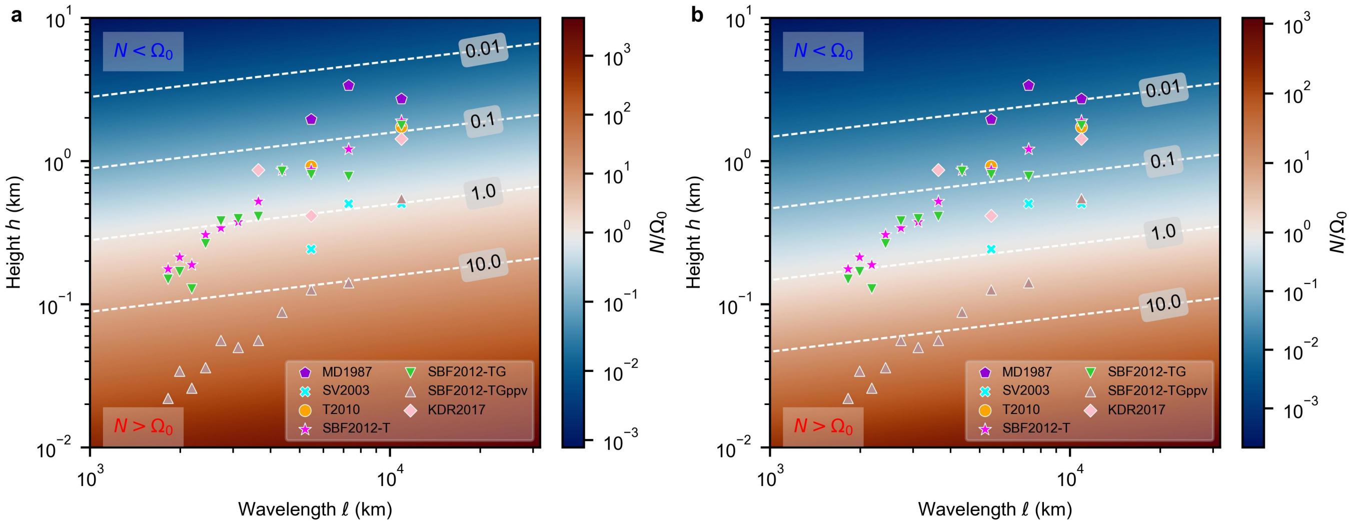

Supplementary Fig. 12: Normalized buoyancy frequency N/Ω_o (color) as a function of the wavelength ℓ and height h of the CMB topography for (**a**) $K_{top} = 0.83$ (upper bound) and (**b**) $K_{top} = 0.23$ (maximum a posteriori estimate). Symbols show the rms of h at different spherical harmonic degrees (converted to ℓ) for a selected set of CMB topography models (MD1987[21]; SV2003[22]; T2010[23]; SBF2012-T & SBF2012-TG & SBF2012-TGppv[16]; KDR2017[24])

12 Dynamical models of the geoid at the CMB

Supplementary Fig. 13 shows time snapshots of maps of the topography of the geoid at the CMB obtained from three-dimensional numerical models of mantle convection in spherical geometry. These are from the calculations presented in ref.[20] using the code stagYY[25]. CMB geoid maps for several calculations are shown. The left column shows results for isochemical, purely thermal convection models, and for different viscosity ratios $\Delta\eta_{pPv}$ of the postperovskite (pPv) phase compared to bridgmanite. These corresponds to cases T1–T4 of ref.[20]. Lenses of pPv (of a few hundred kilometers in thickness above the CMB) form in cold, downwelling regions. A reduced viscosity of the pPv leads to an overall decrease of the radial stress at the CMB that can be maintained by mantle flow, leading to a decrease in the amplitude of the topography of the CMB. The latter implies a smaller mass anomaly (from the density contrast between the core and mantle densities), and thus a smaller amplitude of the gravitational potential at the CMB (i.e. a smaller CMB geoid). The right column shows the results for models which include a reservoir of chemically distinct and denser material. These accumulate into thermo-chemical piles in upwelling regions at the bottom of the mantle, and represent chemically distinct LLVPs. These corresponds to cases TC1–TC4 of ref.[20]. Maps of the geometry of the thermochemical piles are shown in Supplementary Fig. 14. Because the thermochemical piles are chemically denser, they remain at the bottom of the mantle. However, because they are located in warmer, upwelling regions of the CMB, they are also thermally lighter, such that their effective density is near-neutral. The reduction in the density contrast of these regions (compared to cold, downwelling regions) results is a weaker mantle density anomalies, and thus a weaker gravitational potential at the CMB, leading to an additional decrease in the amplitude of the CMB geoid.

These results show that the amplitude of the CMB geoid tends to decrease both when LLVPs consist of compositionally distinct thermochemical piles and also when the pPv phase has a weaker viscosity than bridgmanite. Extended Data Fig. 6 shows the spherical harmonic degree 2 component of the CMB geoid maps of Supplementary Fig. 13. The peak-to-peak amplitude is equal to a few tens of meters for the thermochemical case with $\Delta\eta_{pPv} = 10^{-3}$, compatible with the peak-to-peak amplitude along the equator that we infer from our Bayesian inversion of the gravitational strength parameter Γ.

Note that the CMB geoid highs are generally aligned with the locations of thermochemical piles in Supplementary Fig. 14 when $\Delta\eta_{pPv} = 1$ and 10^{-1}. However, the alignment is less clear for a greater viscosity contrast ($\Delta\eta_{pPv} = 10^{-2}$ and 10^{-3}).

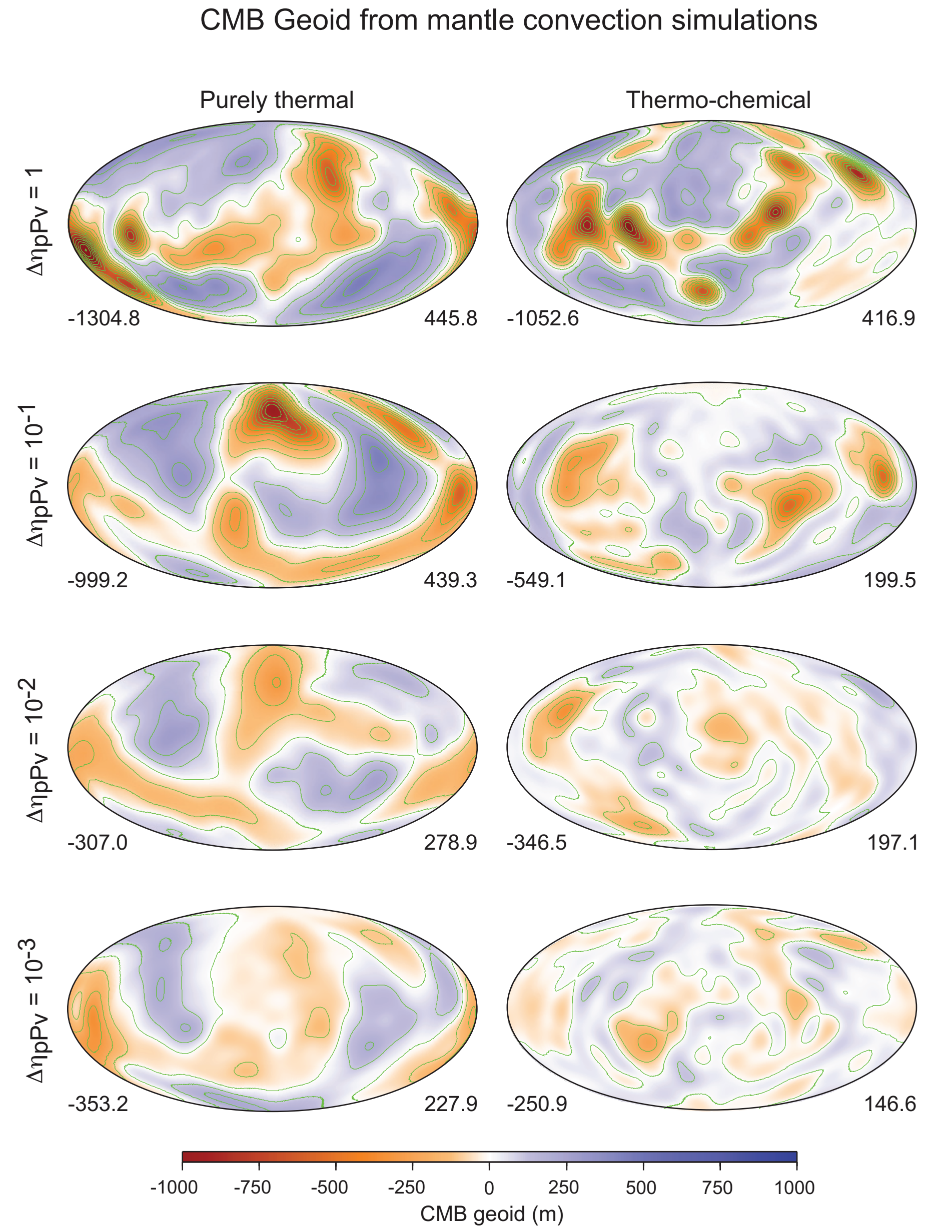

Supplementary Fig. 13: Topography of the geoid at the CMB from purely thermal (left column) and thermochemical (right column) numerical models of mantle convection and for different viscosity ratios of postperovskite versus bridgmanite ($\Delta\eta_{pPv}$, from top to bottom rows: 1, 10^{-1}, 10^{-2}, 10^{-3}). The minimum and maximum geoid heights are indicated at the bottom left and right of each maps. Figure from unpublished material provided by F. Deschamps, with permission.

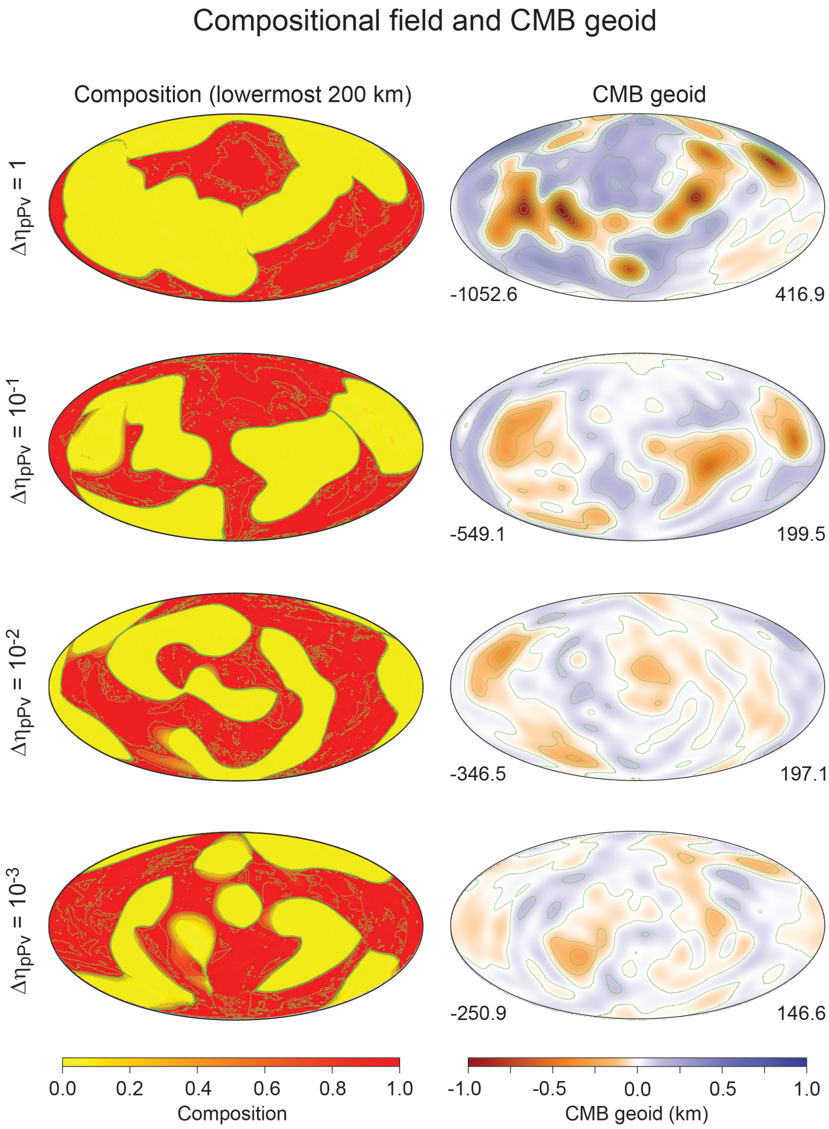

Supplementary Fig. 14: Comparison between the maps of chemically distinct (and denser) material in the bottommost 200 km of the mantle (left column) and the geoid maps (right column) for the thermochemical calculations shown in Supplementary Fig. 13. Figure from unpublished material provided by F. Deschamps, with permission.

13 The core-mantle torque at decadal and shorter timescales

Our study focuses on the core-mantle torque that explains the multidecadal LOD changes. This is primarily because of the limited temporal resolution of the seismically inferred inner core rotation history model of ref.[7]. The best fitting relaxation time τ of the inner core that we find (best fitting vales of 10.2 yr and 7.8 yr for EM and topographic coupling, respectively), however, have implications for the torque balance at shorter timescale.

To illustrate this, Supplementary Fig. 15a shows a synthetic model of fluctuations in inner core rotation rate Ω_i generated by a Gauss-Markov process. It includes multidecadal fluctuations, but also fluctuations at shorter timescales. The change in the longitudinal angle (α) of the long equatorial axis of the ICB topography driven by Ω_i is

$$\frac{d\alpha}{dt} = \Omega_\mathrm{i} - \frac{\alpha}{\tau}\,. \tag{S10}$$

Supplementary Fig. 15b shows the resulting time-history of α for three choices of τ: 80, 10 and 1 yr. The longer τ is, the larger the amplitude of α is, and the more the short frequency component of α gets filtered. For $\tau = 10$ yr (approximately our best fit value for EM coupling), α contains the broad multidecadal changes featured in Ω_{i}, but all fluctuations with a period of 10 yr or shorter are effectively filtered out. Fluctuations in the period range of 10–30 yr remain present but have a weak amplitude.

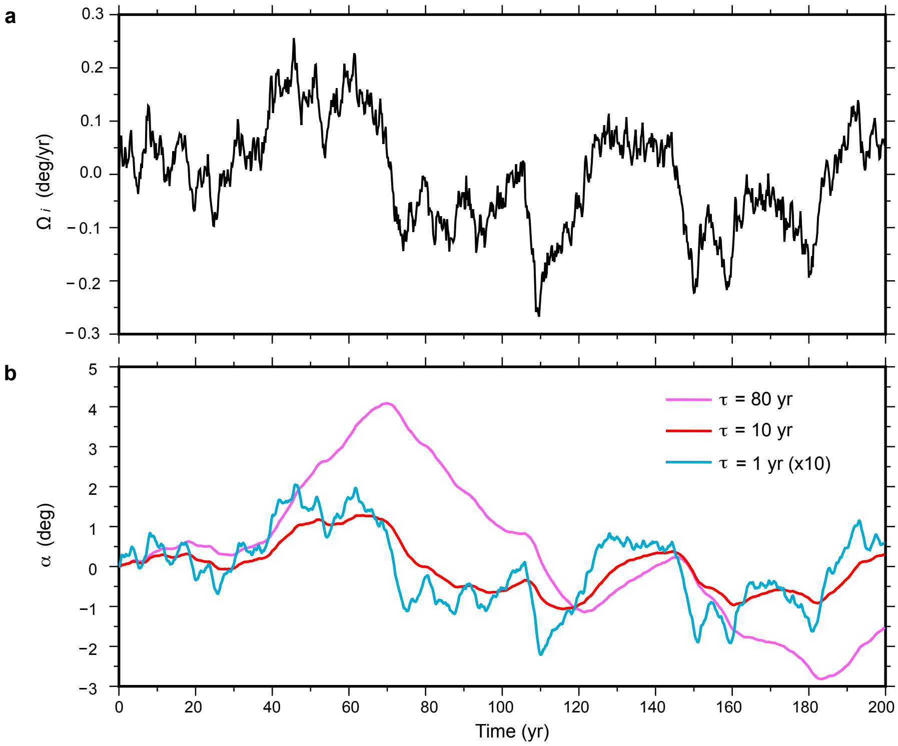

Supplementary Fig. 15: (**a**) Synthetic model of fluctuations of Ω_{i} and (**b**) resulting fluctuations of α for different choices of τ. The results for $\tau = 1$ yr have been multiplied by a factor 10 to improve visualization.

Since the gravitational torque (Γ_{g}) involves a product of the gravitational constant Γ and α, this implies that, for $\tau \sim 10\,\mathrm{yr}$, the gravitational torque becomes ineffective at periods of 10 yr and shorter. Hence, this implies that the core-mantle torque that drives LOD changes at periods of 10 yr or shorter should be dominated by the torque at the CMB (EM or topographic). Likewise, the 6 yr LOD signal of core origin[26] should also be driven by a CMB torque. This is precisely the scenario that is found in numerical simulations approaching Earth conditions[27], where the gravitational torque is also observed to be ineffective at periods shorter than τ.

Our results suggest that the multidecadal torque on the mantle is driven by the gravitational torque. There is thus a cutoff period below which the CMB torque dominates. This cutoff period is difficult to pinpoint precisely, but given the similar magnitudes of the gravitational and CMB torques at long period, and that the amplitude of α is already reduced at periods of ~30 yr, this suggests that LOD changes at periods of ~30 yr and shorter are driven primarily by the CMB torque.

To confirm this, it must be shown that a prediction of the EM and/or topographic torques is indeed consistent with the torque required to explain the ΔLOD in the period range of 10 to 30 yr. However, the predictions based on the flow model of ref.[4] do not contain large fluctuations in this period range. This is shown in Fig. 1b, which we reproduce for convenience in Supplementary Fig. 16. The grey curve shows the torque required on the mantle to explain the shorter timescale ΔLOD variations. The blue curve shows the prediction of the EM torque built from the ensemble solution of the flow model of ref.[4] and based on our best fit mantle conductance of $G = 1.08 \times 10^8$ S. The EM torque prediction does not contain large fluctuations at interdecadal periods. Larger torque amplitudes can be generated with a larger conductance (of the order of 2×10^9 S in order to explain the required torque[28]) but the short period changes of the EM torque prediction do not match well those of the required torque. An analysis of the topographic torque yields a similar conclusion. This could point either to a limitation in the flow model, or indicate that the coupling models at the CMB are incomplete.

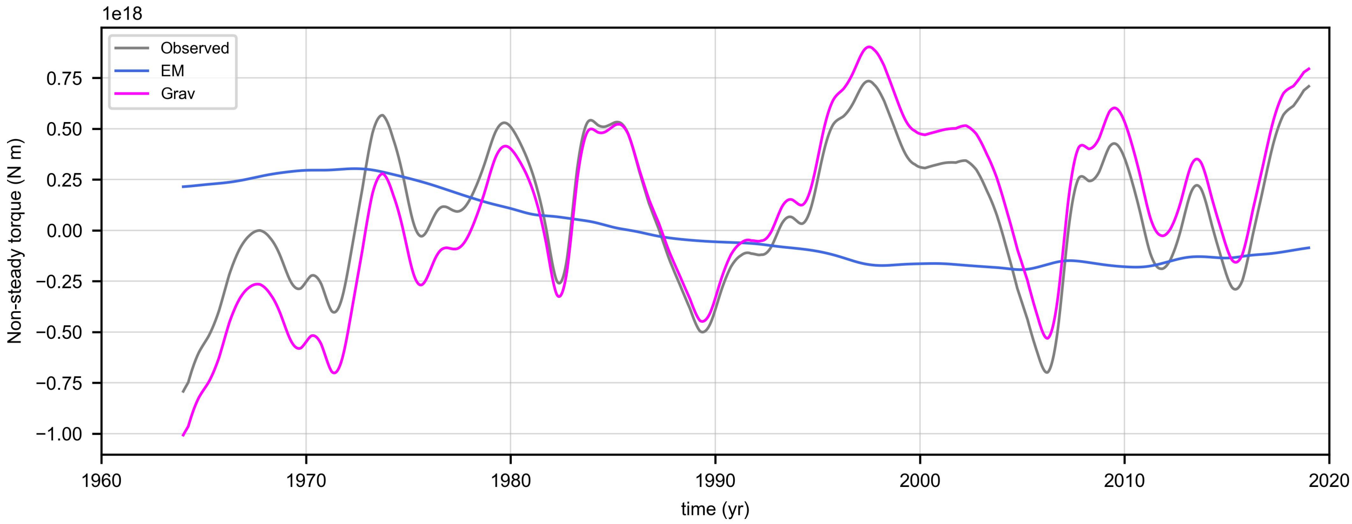

Supplementary Fig. 16: The gravitational torque (magenta) required to explain the torque on the mantle that explains the observed ΔLOD (grey) after removing the EM torque (blue; with conductance $G = 1.08 \times 10^8$ S).

If the gravitational torque was responsible for the shorter period ΔLOD, we can investigate the requirement on the differential inner core rotation. We build a time series of angular positions of the inner core relative to the mantle that would account for the observed torque, $\Gamma_{\rm obs}$, connected to ΔLOD by

$$\Gamma_{\rm obs} = C_{\rm m}\frac{\rm d}{{\rm d}t}\Omega_{\rm m} = -\frac{{\Omega_{\rm o}}^2 C_{\rm m}}{2\pi}\frac{\rm d}{{\rm d}t}\Delta{\rm LOD}\,, \tag{S11}$$

where $C_{\rm m}$ is the moment of inertia of the mantle, $\Omega_{\rm o}$ is Earth's mean rotation rate. The gravitational torque required to explain the ΔLOD in Supplementary Fig. 16 is $\Gamma_{\rm g} = \Gamma_{\rm obs} - \Gamma_{\rm em}$ and is shown by the magenta curve.

Using $\Gamma_{\rm g} = \Gamma\alpha$, applying the operator $({\rm d}/{\rm d}t + 1/\tau)$ on each side, and using Eq. (S10), the prediction of the changes in inner core rotation $\Omega_{\rm i}$ and its associated change in angular rotation angle $\phi_{\rm i}$ is

$$\Omega_{\rm i} = \frac{{\rm d}\phi_{\rm i}}{{\rm d}t} = \frac{1}{\Gamma}\left(\frac{\rm d}{{\rm d}t} + \frac{1}{\tau}\right)\Gamma_{\rm g}(t)\,. \tag{S12}$$

Supplementary Fig. 17 shows (light blue curve) the predicted changes in $\phi_{\rm i}$ from a numerical integration of Eq. (S12) and using our best-fit values of $\Gamma = 1.4 \times 10^{19}$ N m and $\tau = 10.2$ yr. We also show a prediction (dashed curve) obtained by neglecting altogether the contribution from the EM torque, which can be computed simply from

$$\phi_{\rm i} = -\frac{{\Omega_{\rm o}}^2}{2\pi}\frac{C_{\rm m}}{\Gamma}\left(\frac{\rm d}{{\rm d}t} + \frac{1}{\tau}\right)\Delta{\rm LOD}\,. \tag{S13}$$

The peak-to-peak changes in the predicted $\phi_{\rm i}$ over a period of 10 yr are approximately 5°. We also plot on Supplementary Fig. 17 the seismically inferred $\phi_{\rm i}$ from ref.[7] which we have used in our study and from the more recent results of ref.[29]. The short period changes in the predicted $\phi_{\rm i}$ generally fits within the scatter in the data from this latter study (although barely), and on this ground one could argue that the predicted $\phi_{\rm i}$ is not inconsistent with it. Adopting a larger value of Γ (within our 95% CI) would reduce the amplitude of the predicted $\phi_{\rm i}$, making it more compatible with the scatter in the data. However, the data show no clear hint of a short period signal that resembles this ϕ_i prediction. Furthermore, the rapid changes in ϕ_i imply very large fluctuations in Ω_i predicted from Eq. (S12). Supplementary Fig. 18 shows this prediction, which includes fluctuations as large as 2 to 3 °/yr over a few years. This corresponds to rotational speeds at the equator of the inner core of 40 to 60 km/yr, two orders of magnitude larger than the typical changes in zonal core flow at the CMB at subdecadal timescales[30]. While the changes in inner core rotation are driven by zonal core flow at the ICB, which are not directly accessible, we do not expect such an enormous contrast between the zonal flow fluctuations at the ICB versus those at the CMB. Hence, on this ground, it appears unlikely that the short-period ΔLOD are driven by the gravitational torque, as it requires changes in Ω_i that are too large. Consequently, the short-period ΔLOD are most likely driven by a torque at the CMB, even though this remains to be properly demonstrated.

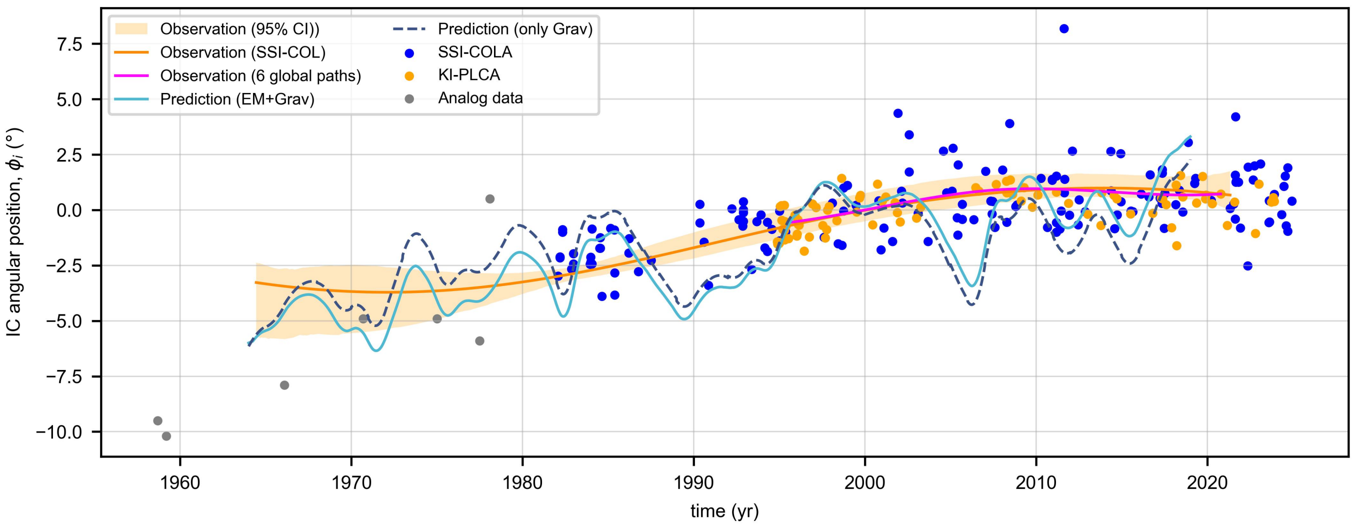

Supplementary Fig. 17: Comparison between the seismic inferences of the inner-core angular position from ref.[29] (blue, orange and grey dots) and ref.[7] (orange and magenta curves, with shaded envelopes) and the predictions based on Eqs. (S12) (light blue curve) and (S13) (dashed black curve) based on our best-fit torque parameters.

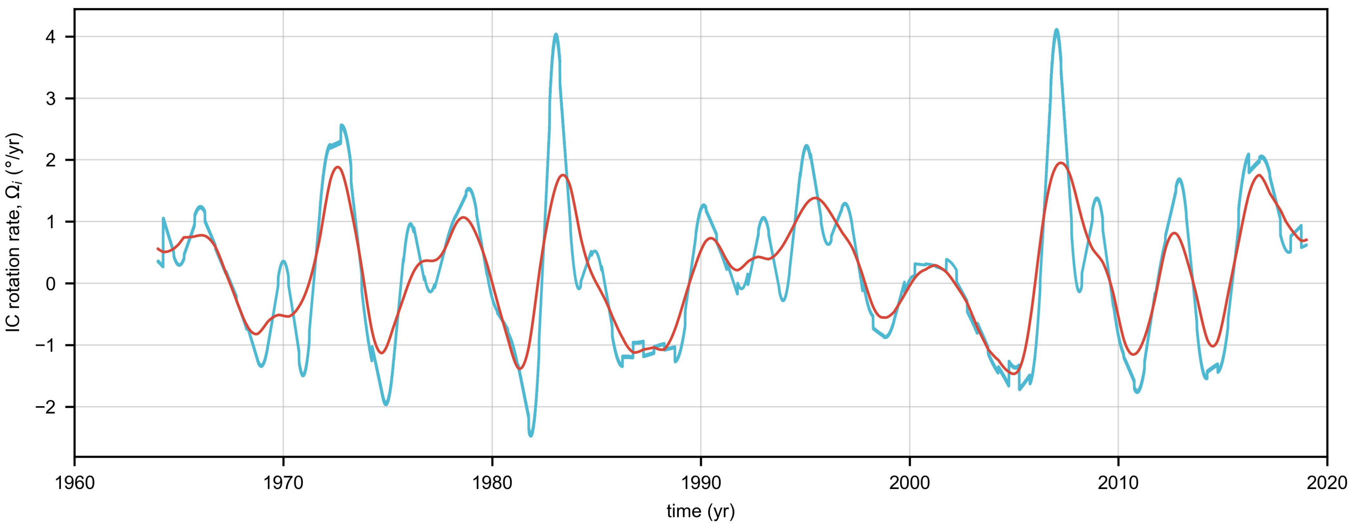

Supplementary Fig. 18: Changes in the inner-core rotation rate Ω_i (blue) derived from the required gravitational torque shown in Supplementary Fig. 16 using $\Gamma = 1.4 \times 10^{19}$ N m and $\tau = 10.2$ yr. The orange curve corresponds to a 2-year running average.

References

[1] L. V. Morrison, F. R. Stephenson, C. Y. Hohenkerk, and M. Zawilski. Addendum 2020 to 'measurement of the Earth's rotation: 720 BC to AD 2015'. *Proc. R. Soc. A*, 477:20200776, 2021.

[2] J. G. Williams and D. H. Boggs. Secular tidal changes in lunar orbit and Earth rotation. *Celest. Mech. Dyn. Astron.*, 126:89–129, 2016.

[3] M. K. Shahvandi, S. Adhikari, M. Dumberry, S. Mishra, and B. Soja. The increasingly dominant role of climate change on length of day variations. *Proc. Natl Acad. Sci. USA*, 121:e2406930121, 2024.

[4] M. Istas, N. Gillet, C. C. Finlay, M. D. Hammer, and L. Huder. Transient core surface dynamics from ground and satellite geomagnetic data. *Geophys. J. Int.*, 233(3):1890–1915, 2023.

[5] L. Huder, N. Gillet, C. C. Finlay, M. D. Hammer, and H. Tchoungui. COV-OBS.x2: 180 years of geomagnetic field evolution from ground-based and satellite observations. *Earth Planets Space*, 72(160), 2020.

[6] L. Huder, N. Gillet, and F. Thollard. pygeodyn 1.1.0: a Python package for geomagnetic data assimilation. *Geosci. Model Dev.*, 12:3795–3803, 2019.

[7] Y. Yang and X. Song. Multidecadal variation of the Earth's inner-core rotation. *Nat. Geosci.*, 16:182–187, 2023.

[8] A. Gelman and D. B. Rubin. A single series from the Gibbs sampler provides a false sense of security. In J. M. et al. Bernardo, editor, *Bayesian Statistics 4*, pages 652–631. Oxford University Press, 1992.

[9] A. Vehtari, A. Gelman, D. Simpson, B. Carpenter, and P.-C. Bürkner. Rank-normalization, folding, and localization: an improved $\hat{R}$ for assessing convergence of MCMC (with discussion). *Bayesian Anal.*, 16:667–718, 2021.

[10] R. E. Kass, B. P. Carlin, A. Gelman, and R. M. Neal. Markov Chain Monte Carlo in practice: a roundtable discussion. *Am. Stat.*, 52:93–100, 1998.

[11] A. Gelman, J. B. Carlin, H. S. Stern, D. B. Dunson, A. Vehtari, and D. B. Rubin. *Bayesian Data Analysis*. Chapman and Hall/CRC, 2013.

[12] N. Gillet, F. Gerick, D. Jault, T. Schwaiger, J. Aubert, and M. Istas. Satellite magnetic data reveal interannual waves in Earth's core. *Proc. Natl Acad. Sci. USA*, 119(13):e2115258119, 2022.

[13] N. Gillet, L. Huder, and J. Aubert. A reduced stochastic model of core surface dynamics based on geodynamo simulations. *Geophys. J. Int.*, 219(1):522–539, 2019.

[14] R. Monville, D. Cébron, and D. Jault. Topographic drag at the core-mantle interface. *J. Geophys. Res. Solid Earth*, 130:e2023JB029770, 2025.

[15] P. Koelemeijer. Toward consistent seismological models of the core-mantle boundary landscape. In H. Marquardt, M. Ballmer, S. Cottaar, and J. Konter, editors, *Mantle convection and surface expressions*, chapter 9. AGU monograph, 2021.

[16] G. Soldati, L. Boschi, and A. Forte. Tomography of core-mantle boundary and lowermost mantle coupled by geodynamics. *Geophys. J. Int.*, 189:730–746, 2012.

[17] M. W. Ammann, J. P. Brodholt, J. Wookey, and D. P. Dobson. First-principles constraints on diffusion in lower-mantle minerals and a weak D" layer. *Nature*, 465:462–465, 2010.

[18] J. W. Hernlund, C. Thomas, and P. J. Tackley. A doubling of the post-perovskite phase boundary and structure of the Earth's lowermost mantle. *Nature*, 434:882–886, 2005.

[19] J. W. Hernlund and A. K. McNamara. The core-mantle boundary region. In G. Schubert, editor, *Treatise on Geophysics*, volume 7, chapter 11, pages 461–519. Elsevier, Oxford, 2015.

[20] F. Deschamps and Y. Li. Core-mantle boundary dynamic topography: Influence of postperovskite viscosity. *J. Geophys. Res. Solid Earth*, 124:9247–9264, 2019.

[21] A. Morelli and A. Dziewonski. Topography of the core-mantle boundary and lateral homogeneity of the liquid core. *Nature*, 325:678–683, 1987.

[22] E. Sze and R. van der Hilst. Core mantle boundary topography from short period PcP, PKP, and PKKP data. *Phys. Earth Planet. Inter.*, 135:27–46, 2003.

[23] S. Tanaka. Constraints on the core-mantle boundary topography from P4KP-PcP differential travel times. *J. Geophys. Res.*, 115:B04310, 2010.

[24] P. Koelemeijer, A. Deuss, and J. Ritsema. Density structure of Earth's lowermost mantle from Stoneley mode splitting observations. *Nat. Commun.*, 8:15241, 2017.

[25] P. J. Tackley. Modelling compressible mantle convection with large viscosity contrasts in a three-dimensional spherical shell using the yin-yang grid. *Phys. Earth Planet. Inter.*, 171:7–18, 2008.

[26] S. Rosat and N. Gillet. Intradecadal variations in the length of day: Coherence with models of the Earth's core dynamics. *Phys. Earth Planet. Inter.*, 341:107053, 2023.

[27] J. Aubert. Geodynamo simulations spanning millennia in the physical conditions of Earth's core. *J. Stud. Earth's Deep Inter.*, 2:3, 2026.

[28] N. Gillet, D. Jault, and E. Canet. Excitation of traveling torsional normal modes in an Earth's core model. *Geophys. J. Int.*, 210:1503–1516, 2017.

[29] K. Wu, X. Song, and Y. Yang. Pattern of inner-core differential rotation from long-term earthquake sequences and USArray network. *Geophys. Res. Lett.*, 53:e2025GL119295, 2026.

[30] N. Gillet, D. Jault, E. Canet, and A. Fournier. Fast torsional waves and strong magnetic field within the Earth's core. *Nature*, 465:74–77, 2010.